

Correlation Induced Magnetic Topological Phases in Mixed-Valence Compound SmB_6

Huimei Liu,^{1,2} Moritz M. Hirschmann,² George A. Sawatzky,^{3,4} Giniyat Khaliullin,² and Andreas P. Schnyder²

¹*Institute for Theoretical Solid State Physics and Würzburg-Dresden Cluster of Excellence ct.qmat, IFW Dresden, Helmholtzstr. 20, 01069 Dresden, Germany*

²*Max Planck Institute for Solid State Research, Heisenbergstrasse 1, D-70569 Stuttgart, Germany*

³*Department of Physics and Astronomy, University of British Columbia, Vancouver B.C. V6T 1Z1, Canada*

⁴*Stewart Blusson Quantum Matter Institute, University of British Columbia, Vancouver B.C. V6T 1Z4, Canada*

(Dated: November 30, 2023)

SmB_6 is a mixed-valence compound with flat f -electron bands that have a propensity to magnetism. Here, using a realistic Γ_8 quartet model, we investigate the dynamical spin susceptibility and describe the in-gap collective mode observed in neutron scattering experiments. We show that as the Sm valence increases with pressure, the magnetic correlations enhance and SmB_6 undergoes a first-order phase transition into a metallic antiferromagnetic state, whose symmetry depends on the model parameters. The magnetic orderings give rise to distinct band topologies: while the A-type order leads to an overlap between valence and conduction bands in the form of Dirac nodal lines, the G-type order has a negative indirect gap with weak \mathbb{Z}_2 indices. We also consider the spin polarized phase under a strong magnetic field, and find that it exhibits Weyl points as well as nodal lines close to the Fermi level. The magnetic phases show markedly different surface states and tunable bulk transport properties, with important implications for experiments. Our theory predicts that a magnetic order can be stabilized also by lifting the Γ_8 cubic symmetry, thus explaining the surface magnetism reported in SmB_6 .

In the recent years, the fields of band topology [1] and heavy fermions [2] have intertwined to form the new research direction of topological heavy-fermion materials [3–13]. These materials exhibit topologically nontrivial band structures together with a number of strong-correlation effects, e.g. non-Fermi liquid behavior, unconventional quantum criticality, and Kondo lattice physics. The interplay between topology and electron correlations creates various novel phenomena, whose robust nature makes them amenable for topological quantum devices [14, 15]. Correlation induced topological properties include exceptional points in quasiparticle spectra [9], giant spontaneous Hall effects [11], and helical magnetism induced by Weyl electrons [12]. Yet another intriguing possibility is that the magnetism of f -electrons may alter the band topology of the charge carriers. This is what we study here in the context of the mixed-valence, heavy-fermion material SmB_6 [16–18].

The electronic structure of SmB_6 is characterized by strongly correlated $4f$ and itinerant $5d$ electrons, whose hybridization opens up a gap at the Fermi level with nontrivial topology [3, 6, 20]. The Sm valence fluctuates between Sm^{2+} and Sm^{3+} states. Its average value v can be tuned by pressure, in favor of magnetic Sm^{3+} with smaller ionic size, as sketched in Fig. 1(a). With increasing Sm valence, SmB_6 undergoes a discontinuous insulator-to-metal transition, accompanied by antiferromagnetic (AFM) order [1, 21–23, 25, 26]. Remarkably, this transition occurs at an intermediate valence, $v_c \sim 2.7$ [1, 25], well before reaching the fully trivalent state, such that valence fluctuations coexist with magnetism. This intriguing phase transition calls for a new theoretical description. In particular, the tunable interplay between band topology and magnetism at intermediate valence may give rise to new types of topological

characteristics with interesting surface properties.

In this Letter, we address the above points based on a realistic model which reproduces the insulating band structure of SmB_6 , as well as gives rise to a low-energy collective spin excitation below the charge gap, manifesting the proximity to magnetic order. In our theory, which explicitly includes the Sm valence v as a tuning parameter, the spin exciton softens and gains intensity as v increases. At a critical value of v_c , an insulator-to-magnetic-metal phase transition of first order takes place. The transition is driven by the exchange interactions between magnetoactive Sm^{3+} ions, whose density increases with pressure. Depending on the model parameters, different AFM states (such as A- or G-type orders) can form. We found that the magnetic phases exhibit band topologies that are markedly different from the insulating nonmagnetic phase. While the A-type order has nodal lines with surface states [27] at the Fermi level, the G-type order shows an indirect negative band gap with weak \mathbb{Z}_2 indices and corresponding Dirac surface states. In the spin polarized phase under a strong magnetic field, SmB_6 becomes a nodal-line Weyl semimetal. We characterize these band topologies by use of mirror Chern numbers, \mathbb{Z}_2 invariants, and a newly introduced “glide-mirror-graded” Wilson loop.

The model.—The SmB_6 crystal has cubic symmetry, with B ions forming an octahedron at the cube center and Sm ions at the cube corners, see Fig. 1(b). A hybridization of the Sm $4f$ orbitals with conduction bands leads to valence fluctuations between nearly degenerate $\text{Sm}^{2+}(f^6)$ and $\text{Sm}^{3+}(f^5)$ states. The resulting wavefunction can effectively be expressed as a coherent superposition $\sqrt{1-n} |f^6; d^0\rangle + \sqrt{n} |f^5; d^1\rangle$, where $|d\rangle$ denotes the Sm $5d$ band states admixed with B $2p$ orbitals, and $n = v - 2$ is the density of the magnetic Sm^{3+} ions.

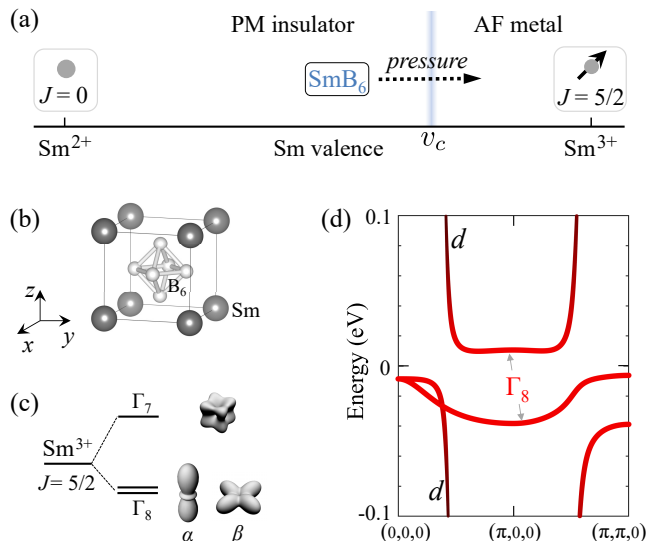


FIG. 1: (a) Sketch of the Sm ionic states and phase behavior of SmB_6 under pressure. (b) Lattice structure of SmB_6 . (c) Crystal field splitting of the $J = 5/2$ multiplet into Γ_8 quartet and Γ_7 doublet. The Γ_8 quartet has a two-fold orbital degeneracy, α and β Kramers doublets with elongated and planar spatial shapes. (d) Low energy band structure of SmB_6 showing an insulating gap at the Fermi level. The black and red colors indicate the contributions from the highly dispersive $5d$ and quasilocalized $4f(\Gamma_8)$ states, respectively.

The $\text{Sm}^{2+}(f^6)$ ion has a $J = 0$ singlet ground state. For Sm^{3+} with the f^5 configuration, the lowest multiplet is the $J = 5/2$ sextet, which is split by the cubic crystal field into a Γ_8 quartet and a Γ_7 doublet, see Fig. 1(c). In SmB_6 , the Γ_7 level is about 20 meV higher in energy [3]. Moreover, the Γ_7 and $5d$ states have a negligible wavefunction overlap. Hence we neglect the Γ_7 excitation, and focus on the Γ_8 quartet, the $J = 0$ singlet of Sm^{2+} , and the $5d$ bands to construct a low-energy Hamiltonian.

By symmetry, the transitions between $f^6(J = 0)$ and $f^5(J = 5/2; \Gamma_8)$ states can be described as the removal/addition of an f -electron with the angular momentum $j = 5/2$ and Γ_8 symmetry. This mapping, which re-scales the bare f -electron hopping amplitudes by the coefficients of fractional parentage [29], leads to the following Hamiltonian:

$$\begin{aligned} \mathcal{H} = & E_d \sum_{i\sigma\gamma} d_{i\sigma\gamma}^\dagger d_{i\sigma\gamma} + \sum_{ij} \sum_{\sigma\gamma\gamma'} t_{d,ij} d_{i\sigma\gamma}^\dagger d_{j\sigma\gamma'} \\ & + E_f \sum_{i\sigma\gamma} f_{i\sigma\gamma}^\dagger f_{i\sigma\gamma} + \sum_{ij} \sum_{\sigma\sigma'\gamma\gamma'} t_{f,ij} f_{i\sigma\gamma}^\dagger f_{j\sigma'\gamma'} \\ & + \sum_{ij} \sum_{\sigma\sigma'\gamma\gamma'} V_{ij} (d_{i\sigma\gamma}^\dagger f_{j\sigma'\gamma'} + \text{H.c.}), \end{aligned} \quad (1)$$

where $d_{i\sigma\gamma}^\dagger$ ($f_{i\sigma\gamma}^\dagger$) denote the creation operators of the $5d$ band (Γ_8 quartet) states on site i with (pseudo)spin σ and orbital index γ . The spin-orbital structure of the matrix elements t_d , t_f , and V follows from the symmetries of

the $5d$ and $4f(\Gamma_8)$ wavefunctions [5, 6] (see Supplemental Material for details [31]). The Γ_8 quartet may be either fully occupied (Sm^{2+}) or host a single-hole (Sm^{3+}). We treat this constraint on a mean-field level, and vary the energy levels E_d and E_f to control the f -hole density $n = v - 2$. The hopping amplitudes, renormalized by the correlation effects, are determined by a fit to experiments [31].

The band structure near the Fermi level, calculated at the valence $v = 2.56$ (i.e. at ambient pressure), is shown in Fig. 1(d). We observe two flat bands originating from the Γ_8 states, and one highly dispersive band of $5d$ character. Their hybridization opens up an insulating band gap of ~ 17 meV, consistent with experiment [32]. The band inversion between the Γ_8 and d bands at the X-point $(\pi, 0, 0)$ leads to a nontrivial strong \mathbb{Z}_2 topology with helical surface states [3, 6, 20].

Spin exciton and magnetic order.—Having the model that reproduces the low-energy electronic states of SmB_6 , we address now its magnetic properties. In SmB_6 , a dispersive magnetic mode is formed inside the charge gap [33]. This is a signature of strong correlations among the $J = 5/2$ moments, which interact via the conduction bands or various superexchange channels (e.g., via the B orbitals). For simplicity, we model these interactions by the isotropic exchange Hamiltonian,

$$\mathcal{H}_{\text{ex}} = \sum_{\langle ij \rangle} \mathcal{J}_{ij} \mathbf{J}_i \cdot \mathbf{J}_j, \quad (2)$$

and calculate the dynamical magnetic susceptibility using the random phase approximation:

$$\chi(\mathbf{q}, \omega) = \frac{\chi_0(\mathbf{q}, \omega)}{1 + \mathcal{J}_q \chi_0(\mathbf{q}, \omega)}. \quad (3)$$

Here, $\mathcal{J}_q = \sum_{\mathbf{R}} \mathcal{J}_{\mathbf{R}} e^{i\mathbf{q} \cdot \mathbf{R}}$ and $\chi_0(\mathbf{q}, \omega)$ is the bare magnetic susceptibility, which can readily be evaluated using the eigenstates and energies of the electronic bands obtained above [31]. The major contribution to $\chi_0(\mathbf{q}, \omega)$ is due to the transitions between the flat bands in Fig. 1(d), which give rise to a gapped Stoner continuum. Of our prime interest is, however, a low-energy collective mode that emerges as a sharp particle-hole bound state inside the gap [33–35]. From Eq. (3), the energy $\omega_{\mathbf{q}}$ of this mode is given by the condition $\mathcal{J}_q = -1/\chi_0'(\mathbf{q}, \omega_{\mathbf{q}})$, and thus sensitive to the exchange parameters.

Having no microscopic theory for exchange interactions in SmB_6 , we consider a minimal set of the \mathcal{J}_{ij} couplings up to third-nearest neighbors. Figure 2(a) shows the spin-exciton peaks in $\chi''(\mathbf{q}, \omega)$, calculated using the parameter set $(\mathcal{J}_1, \mathcal{J}_2, \mathcal{J}_3) = (14.7, 6.5, 2.7)$ meV. The results for $v = 2.56$ qualitatively agree with the inelastic neutron scattering data [33].

We find that the spin exciton mode is highly sensitive to the valence state. It strongly softens and gains a large spectral weight as v increases, see Fig. 2(a). Physically, increasing the density of magnetic Sm^{3+} ions tips the balance between the exchange interactions and the

f -electron delocalization energy, driving the system towards a magnetic instability. SmB_6 develops a long-range AFM order at the critical valence $v_c \sim 2.7$ [1, 25]. To describe this transition, we perform a mean-field calculation for the magnetic order parameter as a function of v . We let the effective hopping parameters (t_d, t_f, V) vary as the valence increases under pressure, and rescale them by a phenomenological factor $[1 + \eta(v - v_0)]$, where $v_0 = 2.56$. Physically, the sign of the parameter η is determined by two competing effects: on the one hand, the effective hoppings are reduced ($\eta < 0$) by the correlations that enhance with valence v ; on the other hand, they increase ($\eta > 0$) due to the increased wavefunction overlap under pressure. With $\eta = 0.6$ [36], a magnetic solution appears at $v_c \simeq 2.7$ via a first-order phase transition, see Fig. 2(b). Once the magnetic order is established, the spin degeneracy is lifted and the band structure gets rearranged, which induces a simultaneous insulator-to-metal transition. The feedback effects between spin order and band structure result in a discontinuous transition, as observed in SmB_6 [21, 23].

It should be noted that the AFM ordering pattern (not yet fully identified experimentally) is decided by the choice of \mathcal{J}_{ij} parameters. While the above \mathcal{J}_{ij} values (motivated by the spin-exciton dispersion fits) support G-type (Néel) state, other structures, such as A-type order suggested by a $(\pi, 0, 0)$ peak in the bare susceptibility $\chi_0(\mathbf{q})$ [31], are possible. Future experiments are required to quantify the exchange Hamiltonian in SmB_6 .

Since the Γ_8 quartet is a spin-orbit entangled object, magnetic order also affects the orbital shape of the f -electron cloud and thus reduces cubic symmetry of the paramagnetic phase. Alternatively, lifting the degeneracy of the α and β states of the Γ_8 quartet [Fig. 1(c)] by uniaxial stress reduces the hybridization gap, triggering thereby magnetic order and an insulator-to-metal transition (Supplemental Material [31]); this is an interesting proposal for experiment. In fact, the Γ_8 quartet splitting is naturally present near the surface as well as near defects, and should be relevant for the analysis of the surface states and transport properties of SmB_6 . For instance, the surface magnetism reported in SmB_6 [9, 10] can be understood as a natural consequence of the cubic symmetry breaking near the surface.

Topological properties.—Paramagnetic SmB_6 is a topological insulator with strong and weak \mathbb{Z}_2 invariants and mirror Chern numbers [3]. Here, we present a topological analysis of the magnetically ordered metallic phases, based upon the Γ_8 quartet model of SmB_6 . Specifically, we consider the two possible magnetic states, namely the A-type and G-type AFM orders shown in Figs. 3(a,b). Our topological analysis is based on symmetries, and therefore applies also, at least qualitatively, to similar antiferromagnetic systems.

In the magnetic phases, the symmorphic symmetries $Pm\bar{3}m$ of the paramagnetic phase are lowered to *non-symmorphic* magnetic space groups (MSG) [39]. For the A-type order we find the tetragonal MSG $P_{2c}4/\text{mm}'\text{m}'$,

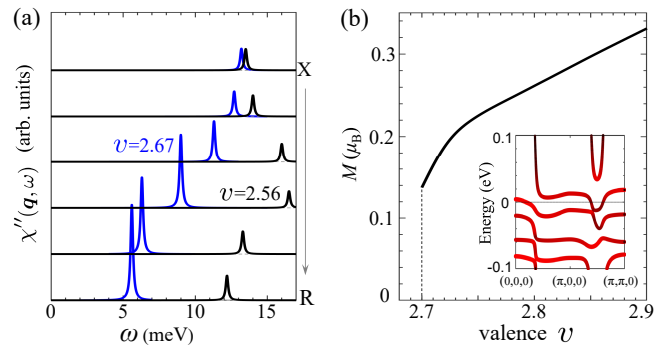


FIG. 2: (a) Dynamical magnetic susceptibility $\chi''(\mathbf{q}, \omega)$ for the valence $v = 2.56$ (black) and 2.67 (blue), for \mathbf{q} values along the high symmetry path from $X = (\pi, 0, 0)$ to $R = (\pi, \pi, \pi)$. The particle-hole continuum (not shown) is above $\simeq 17$ meV. (b) The G-type ordered magnetic moment M as a function of v . The inset shows the metallic band structure at $v = 2.72$.

while for the G-type order the MSG is $P_I4/\text{mm}'\text{m}'$, which is body-centered. Here we adopt the OG convention [39], for which the coordinate basis of the MSG coincides with the parent SG. Both MSGs contain magnetic translations, namely $T_A = Tt(0, 0, 1)$ along the z axis for the A-type order and $T_G = Tt(1, 0, 0)$ along the x axis for the G-type order, where $T = i\sigma_y K$ is the time-reversal operator. We note that T_G is equivalent to T_A up to a lattice vector of the G-type structure. Yet, the converse is not true, i.e., T_A is not equivalent to T_G up to a lattice vector of the A-type lattice.

To study the band topologies of the AFM phases, we compute the surface states and the associated topological numbers in our model, whereby we implement the coupling of the charge carriers to the AFM texture by an on-site Zeeman term. We find that for both AFM orders the bands are Kramers degenerate, due to the presence of both magnetic translations (T_A, T_G) and inversion (P) with $(PT_A)^2 = (PT_G)^2 = -1$. Moreover, both A- and G-type orders exhibit Dirac points below the Fermi level, while the A-type order has in addition nodal lines [31]. We now discuss these two AFM orders in more detail.

(i) The A-type order exhibits Dirac nodal lines in the $k_z = \frac{\pi}{2}$ plane for a large parameter range (due to the wide d -band), see Fig. 3(c). These nodal lines are classified as type II [40], since they are strongly tilted. The appearance of Dirac nodal lines upon entering the A-type order defies the expectation that with less symmetries there are less symmetry-protected crossings. These Dirac nodal lines are protected by the m_z mirror symmetry together with PT_A . In the $k_z = \frac{\pi}{2}$ mirror plane PT_A pairs identical representations of m_z , such that two Kramers pairs with distinct m_z representations can cross in protected nodal lines. These nodal lines can be thought of as generalizations of lines protected by inversion and off-centered mirror symmetry [41, 42].

By the bulk-boundary correspondence, one expects that these nodal lines lead to states localized on the $[001]$

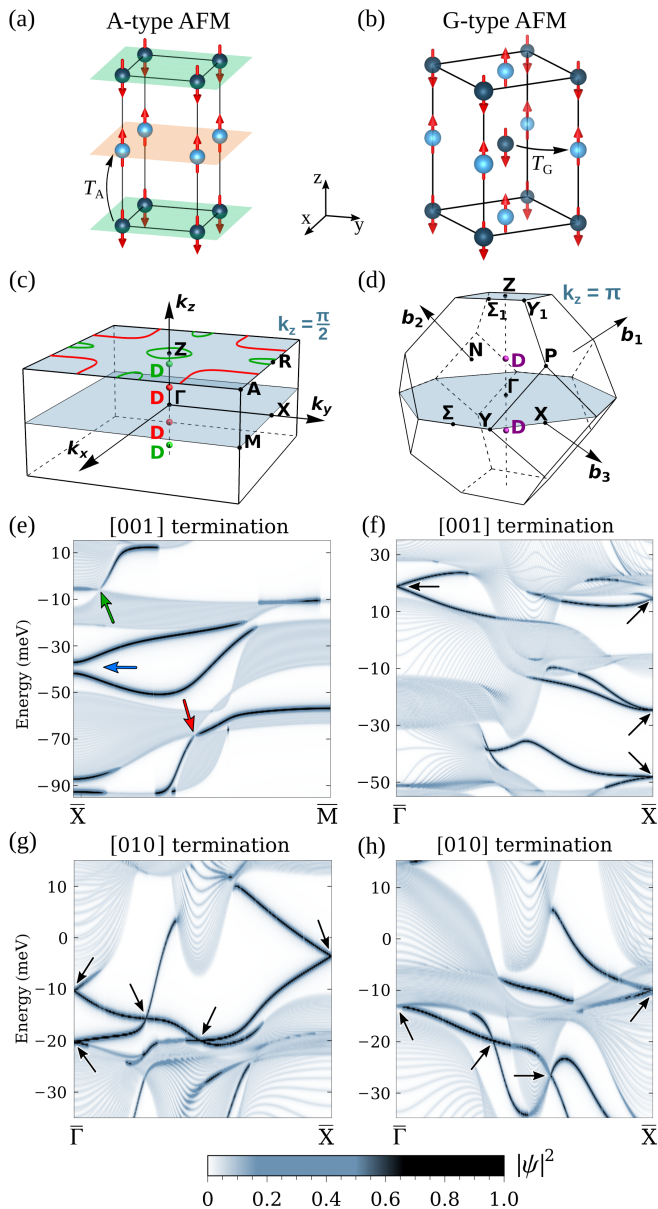


FIG. 3: Band topology of SmB_6 at valence $v = 2.74$ for the A-type (left) and G-type (right) antiferromagnetic states. (a),(b) Magnetic structures with moments indicated by the red arrows. (c),(d) Nodal lines and Dirac points in the vicinity (green) and below (red & purple) the Fermi level. (e-h) Band structures of a 100-layer slab with [001] and [010] termination, respectively. The color scale represents the wave function amplitude of the 10 topmost layers. The arrows mark characteristic features of the different band topologies.

surface. Indeed, Fig. 3(e) shows nodal line surface states for the red and green nodal lines of Fig. 3(c), which however partially merge with bulk bands. In order to characterize the topology of these nodal lines and the associated surface states, one might consider a mirror Berry phase [13, 27]. However, this quantity is unsuitable, because the two orthogonal eigenspaces of the glide mirror symmetries \hat{m}_x and \hat{m}_y exchange along the k_z direc-

tion. Instead, we develop a “glide-mirror graded” Wilson loop [31]. The spectrum of this quantity, which resolves the band degeneracy caused by PT_A , exhibits a qualitative change at the nodal lines, i.e., the emergence of flat bands. Finally, on the [001] surface there appears also a gapped Dirac cone (blue arrow), which can be viewed as a remainder of the paramagnetic surface states, gapped by the magnetic order. While this is similar to an axion insulator [24, 45], a half-integer Hall effect is not expected because of the gapless band structure.

On the [010] surface, on the other hand, there appear no nodal line surface states but only Dirac cones, indicated by black arrows in Fig. 3(g). These Dirac cones, found also in a band structure study [46] of the A-type order, are protected by mirror-Chern numbers and weak \mathbb{Z}_2 invariants defined within the $k_z = 0$ plane [31].

(ii) The G-type order does not have any nodal lines, but only Dirac cones on the Γ -Z axis protected by the fourfold rotation, see Fig. 3(d). Similar to the A-type order, the G-type order has weak \mathbb{Z}_2 invariants in two-dimensional subsystems where $T_G^2 = -1$ [1]. In particular, the three planes $k_x = 0$, $k_y = 0$, and $k_z = 0$, which each contain the time-reversal invariant momenta Γ , X, and Z, have nontrivial weak invariants [31]. By the bulk-boundary correspondence, these weak invariants lead to Dirac cone surface states for the [100], [010], and [001] terminations, see black arrows in Figs. 3(f) and 3(h).

Recent analysis of the quantum oscillation experiments at high magnetic fields suggested the presence of asymmetric nodal lines [47]. Motivated by this proposal, we consider the possibility of nodal lines in the high-field phase of SmB_6 , where the moments are aligned ferromagnetically. In this state, any mirror plane may contain protected accidental nodal lines. Indeed, for the [001] alignment of the magnetic moments we find such nodal lines within the $k_z = 0$ and $k_z = \pi$ mirror planes, in close proximity to the Fermi level. These nodal lines are protected by a quantized π -Berry phase [31].

In conclusion, we have developed a theory for the insulator-to-magnetic-metal transition in SmB_6 . We describe this transition as the softening of an in-gap spin exciton mode, which condenses into an AFM order at the critical density of magnetic Sm^{3+} ions. The AFM order induces a simultaneous insulator-to-metal transition as well as a change in the band topology. Within the Γ_8 quartet model, relevant to SmB_6 , we find that the band structure is transformed from a cubic topological insulator to a tetragonal magnetic metal with symmetry protected Dirac points (G-type order) or Dirac points and nodal lines (A-type order). From our theory, we expect that the magnetic metal exhibits interesting transport characteristics, for example, light- or strain-induced anomalous Hall currents in the A-type order [48–50]. We hope that our findings will spur experimentalists to look for these intriguing properties, and to further characterize the insulator-to-magnetic-metal transition which can be induced in SmB_6 by pressure or uniaxial strain.

We thank Andreas Leonhardt for discussions. G.Kh. thanks the Max Planck-UBC-UTokyo Centre for Quantum Materials at the University of British Columbia, where this work was partially done, for hospitality. H.L. acknowledges support by the Würzburg-Dresden Clus-

ter of Excellence on Complexity and Topology in Quantum Matter *ct.qmat* (EXC 2147, project ID 390858490). A.P.S. thanks the YITP Kyoto for hospitality.

H.L. and M.M.H. contributed equally to this work.

-
- [1] C.-K. Chiu, J. C. Y. Teo, A. P. Schnyder, and S. Ryu, Classification of topological quantum matter with symmetries, *Rev. Mod. Phys.* **88**, 035005 (2016).
- [2] S. Wirth and F. Steglich, Exploring heavy fermions from macroscopic to microscopic length scales, *Nat. Rev. Mater.* **1**, 16051 (2016).
- [3] M. Dzero, K. Sun, V. Galitski, and P. Coleman, Topological Kondo insulators, *Phys. Rev. Lett.* **104**, 106408 (2010).
- [4] P. P. Baruselli and M. Vojta, Scanning tunneling spectroscopy and surface quasiparticle interference in models for the strongly correlated topological insulators SmB_6 and PuB_6 , *Phys. Rev. B* **90**, 201106(R) (2014).
- [5] M. Sundermann, F. Strigari, T. Willers, H. Winkler, A. Prokofiev, J. M. Ablett, J.-P. Rueff, D. Schmitz, E. Weschke, M. M. Sala, *et al.*, CeRu_4Sn_6 : a strongly correlated material with nontrivial topology, *Sci. Rep.* **5**, 17937 (2015).
- [6] P.-Y. Chang, O. Erten, and P. Coleman, Möbius Kondo insulators, *Nat. Phys.* **13**, 794 (2017).
- [7] K. Kimura, T. Yoshida, and N. Kawakami, Topological properties of magnetically ordered heavy-fermion systems in the presence of mirror symmetry, *J. Phys. Soc. Jpn.* **87**, 084705 (2018).
- [8] L. Li, K. Sun, C. Kurdak, and J. W. Allen, Emergent mystery in the Kondo insulator samarium hexaboride, *Nat. Rev. Phys.* **2**, 463 (2020).
- [9] Y. Nagai, Y. Qi, H. Isobe, V. Kozii, and L. Fu, DMFT reveals the Non-Hermitian topology and Fermi arcs in heavy-fermion systems, *Phys. Rev. Lett.* **125**, 227204 (2020).
- [10] M. Klett, S. Ok, D. Riegler, P. Wölfle, R. Thomale, and T. Neupert, Topology and magnetism in the Kondo insulator phase diagram, *Phys. Rev. B* **101**, 161112(R) (2020).
- [11] S. Dzsaber, X. Yan, M. Taupin, G. Eguchi, A. Prokofiev, T. Shiroka, P. Blaha, O. Rubel, S. E. Grefe, H.-H. Lai, *et al.*, Giant spontaneous Hall effect in a nonmagnetic Weyl-Kondo semimetal, *Proc. Natl. Acad. Sci. U.S.A.* **118**, e2013386118 (2021).
- [12] J. Gaudet, H.-Y. Yang, S. Baidya, B. Lu, G. Xu, Y. Zhao, J. A. Rodriguez-Rivera, C. M. Hoffmann, D. E. Graf, D. H. Torchinsky, Weyl-mediated helical magnetism in NdAlSi , *et al.*, *Nat. Mater.* **20**, 1650 (2021).
- [13] S. Wolgast, Y. S. Eo, T. Öztürk, G. Li, Z. Xiang, C. Tinsman, T. Asaba, B. Lawson, F. Yu, J. W. Allen, *et al.*, Magnetotransport measurements of the surface states of samarium hexaboride using Corbino structures, *Phys. Rev. B* **92**, 115110 (2015).
- [14] L. Šmejkal, Y. Mokrousov, B. Yan, and A. H. MacDonald, Topological antiferromagnetic spintronics, *Nat. Phys.* **14**, 242 (2018).
- [15] M. J. Gilbert, Topological electronics, *Commun. Phys.* **4**, 70 (2021).
- [16] A. Menth, E. Buehler, and T. H. Geballe, Magnetic and semiconducting properties of SmB_6 , *Phys. Rev. Lett.* **22**, 295 (1969).
- [17] C. M. Varma, Mixed-valence compounds, *Rev. Mod. Phys.* **48**, 219 (1976).
- [18] P. F. S. Rosa and Z. Fisk, Bulk and Surface Properties of SmB_6 , in *Rare-Earth Borides*, edited by D. S. Inosov (Jenny Stanford, New York, 2021).
- [6] T. Takimoto, SmB_6 : A promising candidate for a topological insulator, *J. Phys. Soc. Jpn.* **80**, 123710 (2011).
- [20] F. Lu, J. Z. Zhao, H. Weng, Z. Fang, and X. Dai, Correlated topological insulators with mixed valence, *Phys. Rev. Lett.* **110**, 096401 (2013).
- [21] A. Barla, J. Derr, J. P. Sanchez, B. Salce, G. Laperot, B. P. Doyle, R. Ruffer, R. Lengsdorf, M. M. Abd-Elmeguid, and J. Flouquet, High-pressure ground state of SmB_6 : electronic conduction and long range magnetic order, *Phys. Rev. Lett.* **94**, 166401 (2005).
- [22] J. Derr, G. Knebel, G. Laperot, B. Salce, M.-A. Méasson, and J. Flouquet, Valence and magnetic ordering in intermediate valence compounds: TmSe versus SmB_6 , *J. Phys.: Condens. Matter* **18**, 2089 (2006).
- [23] J. Derr, G. Knebel, D. Braithwaite, B. Salce, J. Flouquet, K. Flachbart, S. Gabáni, and N. Shitsevalova, From unconventional insulating behavior towards conventional magnetism in the intermediate-valence compound SmB_6 , *Phys. Rev. B* **77**, 193107 (2008).
- [1] N. P. Butch, J. Paglione, P. Chow, Y. M. Xiao, C. A. Marianetti, C. H. Booth, and J. R. Jeffries, Pressure-resistant intermediate valence in the Kondo insulator SmB_6 , *Phys. Rev. Lett.* **116**, 156401 (2016).
- [25] N. Emi, N. Kawamura, M. Mizumaki, T. Koyama, N. Ishimatsu, G. Pristáš, T. Kagayama, K. Shimizu, Y. Osanai, F. Iga, *et al.*, Kondo-like behavior near the magnetic instability in SmB_6 : Temperature and pressure dependences of the Sm valence, *Phys. Rev. B* **97**, 161116(R) (2018).
- [26] Y. Zhou, Q. Wua, P. F. S. Rosa, R. Yu, J. Guo, W. Yi, S. Zhang, Z. Wang, H. Wang, S. Cai, *et al.*, Quantum phase transition and destruction of Kondo effect in pressurized SmB_6 , *Sci. Bull.* **62**, 1439 (2017).
- [27] Y.-H. Chan, C.-K. Chiu, M. Y. Chou, and A. P. Schnyder, Ca_3P_2 and other topological semimetals with line nodes and drumhead surface states, *Phys. Rev. B* **93**, 205132 (2016).
- [3] A. Amorese, O. Stockert, K. Kummer, N. B. Brookes, D.-J. Kim, Z. Fisk, M. W. Haverkort, P. Thalmeier, L. H. Tjeng, and A. Severing, Resonant inelastic x-ray scattering investigation of the crystal-field splitting of Sm^{3+} in SmB_6 , *Phys. Rev. B* **100**, 241107(R) (2019).
- [29] G. Sawatzky and R. Green, The explicit role of anion states in high-valence metal oxides, in *Quantum Materials: Experiments and Theory*, edited by E. Pavarini, E. Koch, J. van den Brink, and G. Sawatzky

- (Forschungszentrum Jülich, 2016, ISBN 978-3-95806-159-0).
- [5] K. Takegahara, Y. Aoki, and A. Yanase, Slater-Koster tables for f electrons, *J. Phys. C: Solid State Phys.* **13**, 583 (1980).
- [31] See Supplemental Material at *** for details of the tight-binding model fits, the calculation of the magnetic susceptibility, the discussion of the mirror-graded Wilson loop, and the analysis of the band topology.
- [32] M. Neupane, N. Alidoust, S.-Y. Xu, T. Kondo, Y. Ishida, D. J. Kim, C. Liu, I. Belopolski, Y. J. Jo, T.-R. Chang, *et al.*, Surface electronic structure of the topological Kondo-insulator candidate correlated electron system SmB_6 , *Nat. Commun.* **4**, 2991 (2013).
- [33] W. T. Fuhrman, J. Leiner, P. Nikolić, G. E. Granroth, M. B. Stone, M. D. Lumsden, L. DeBeer-Schmitt, P. A. Alekseev, J.-M. Mignot, S. M. Koohpayeh, *et al.*, Interaction driven subgap spin exciton in the Kondo insulator SmB_6 , *Phys. Rev. Lett.* **114**, 036401 (2015).
- [34] P. S. Riseborough, Heavy fermion semiconductors, *Ann. Phys. (Leipzig)* **9**, 813 (2000).
- [35] J. Knolle and N. R. Cooper, Excitons in topological Kondo insulators: theory of thermodynamic and transport anomalies in SmB_6 , *Phys. Rev. Lett.* **118**, 096604 (2017).
- [36] The value $\eta = 0.6$ leads to an increase of the hopping parameters by 8% at the critical pressure of $P \sim 6$ GPa, which sounds plausible.
- [37] Y. Nakajima, P. Syers, X. Wang, R. Wang, and J. Paglione, One-dimensional edge state transport in a topological Kondo insulator, *Nat. Phys.* **12**, 213 (2016).
- [38] A. Aishwarya, Z. Cai, A. Raghavan, M. Romanelli, X. Wang, X. Li, G. D. Gu, M. Hirsbrunner, T. Hughes, F. Liu, L. Jiao, and V. Madhavan, Spin-selective tunneling from nanowires of the candidate topological Kondo insulator SmB_6 , *Science* **377**, 1218 (2022).
- [39] S. V. Gallego, E. S. Tasci, G. Flor, J. M. Perez-Mato, and M. I. Aroyo, Magnetic symmetry in the bilbao crystallographic server: a computer program to provide systematic absences of magnetic neutron diffraction, *J. Appl. Cryst.* **45**, 1236 (2012).
- [40] S. Li, Z.-M. Yu, Y. Liu, S. Guan, S.-S. Wang, X. Zhang, Y. Yao, and S. A. Yang, Type-II nodal loops: Theory and material realization, *Phys. Rev. B* **96**, 081106(R) (2017).
- [41] B.-J. Yang, T. A. Bojesen, T. Morimoto, and A. Furusaki, Topological semimetals protected by off-centered symmetries in nonsymmorphic crystals, *Phys. Rev. B* **95**, 075135 (2017).
- [42] J. Zhang, Y.-H. Chan, C.-K. Chiu, M. G. Vergniory, L. M. Schoop, and A. P. Schnyder, Topological band crossings in hexagonal materials, *Phys. Rev. Mater.* **2**, 074201 (2018).
- [13] F. Zhang, C. L. Kane, and E. J. Mele, Topological mirror superconductivity, *Phys. Rev. Lett.* **111**, 056403 (2013).
- [24] R. S. K. Mong, A. M. Essin, and J. E. Moore, Antiferromagnetic topological insulators, *Phys. Rev. B* **81**, 245209 (2010).
- [45] C. Liu, Y. Wang, H. Li, Y. Wu, Y. Li, J. Li, K. He, Y. Xu, J. Zhang, and Y. Wang, Robust axion insulator and Chern insulator phases in a two-dimensional antiferromagnetic topological insulator, *Nat. Mater.* **19**, 522 (2020).
- [46] K.-W. Chang and P.-J. Chen, Anomalous Z_2 antiferromagnetic topological phase in pressurized SmB_6 , *Phys. Rev. B* **97**, 195145 (2018).
- [47] N. Harrison, Highly asymmetric nodal semimetal in bulk SmB_6 , *Phys. Rev. Lett.* **121**, 026602 (2018).
- [48] W. B. Rui, Y. X. Zhao, and A. P. Schnyder, Topological transport in Dirac nodal-line semimetals, *Phys. Rev. B* **97**, 161113(R) (2018).
- [49] T. Matsushita, S. Fujimoto, and A. P. Schnyder, Topological piezoelectric effect and parity anomaly in nodal line semimetals, *Phys. Rev. Research* **2**, 043311 (2020).
- [50] T. Oka and H. Aoki, Photovoltaic Hall effect in graphene, *Phys. Rev. B* **79**, 081406(R) (2009).

Supplemental Material for Correlation Induced Magnetic Topological Phases in Mixed-Valence Compound SmB_6

Here we present the details of the electronic model (Sec. SI), calculation of the magnetic susceptibility (Sec. SII), and consider tetragonal crystal field effect on the phase transition (Sec. SIII). In Sec. SIV, we discuss suitable topological invariants and introduce a glide-mirror graded Wilson loop. Using these invariants, we analyze in Sec. SV the topological properties of SmB_6 in different phases.

SI. Valence states and the tight-binding model

SmB_6 is a prototypical intermediate valence compound, where the ionic charge configuration fluctuates between two different valence states, which are energetically close and coherently superposed in the ground state wavefunction. As illustrated in Fig. S1, the average Sm valence in SmB_6 is “in-between” the divalent and trivalent states, and it can be tuned by external or chemical pressure thanks to the different radii of $\text{Sm}^{2+}(4f^6)$ and $\text{Sm}^{3+}(4f^5)$ ions, the latter being smaller because of the smaller number of $4f$ electrons.

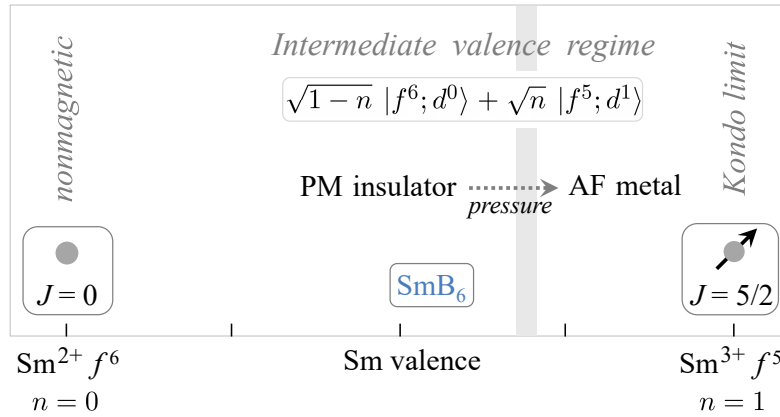


FIG. S1: Schematic of the lowest spin-orbit J multiplets of Sm^{2+} and Sm^{3+} ions in SmB_6 . These two valence states are almost evenly presented in the ground state wavefunction, with the average densities $1 - n \simeq 0.44$ and $n \simeq 0.56$, respectively. As the density of magnetic ions Sm^{3+} is slightly increased (to $n \sim 0.7$ [1]) under pressure, a first order phase transition from nonmagnetic-insulator to magnetic-metal takes place.

Microscopically, the valence fluctuations are caused by hybridization of the $4f$ electrons with $5d$ conduction band states, a process which can schematically be expressed as $f^6 d^0 \Leftrightarrow f^5 d^1$. Both valence states of the Sm ion, $f^6(L = 3, S = 3)$ and $f^5(L = 5, S = 5/2)$, have a number of spin-orbit multiplet levels with total angular momentum $J = 0, 1, \dots$ and $J = 5/2, 7/2, \dots$, respectively. The general Hamiltonian including all these states is obviously complex, but the transitions between the lowest $f^6(J = 0)$ singlet and $f^5(J = 5/2)$ states of interest can be described as the removal/addition of an f -electron with the angular momentum $j = 5/2$. In other words, thanks to the trivial $J = 0$ ground state of Sm^{2+} ion, we can express the valence fluctuations in terms of the hoppings of a single f electron, with the effective amplitudes reduced by the coefficients of fractional parentage [2]. As we neglect the higher-lying Γ_7 level of Sm^{3+} [3] in our model, the $f(j = 5/2)$ electron has to be in the Γ_8 state as well.

The Γ_8 quartet of f electron can be represented by two Kramers doublets, which we denote by α and β ; their wave functions, written in terms of the $j = 5/2$ angular momentum projections, read as follows:

$$|\alpha_{\pm}\rangle = |\pm \frac{1}{2}\rangle, \quad |\beta_{\pm}\rangle = \sqrt{\frac{5}{6}} |\pm \frac{5}{2}\rangle + \sqrt{\frac{1}{6}} |\mp \frac{3}{2}\rangle, \quad (\text{S1})$$

where the subscript \pm denotes the pseudospin-1/2 index. To calculate hopping integrals between these states and d orbitals, one actually needs to express the above $|j_z\rangle$ functions in terms of the f orbital $l = 3$ and spin $s = 1/2$

angular momentum projections $|l_z, s_z\rangle$:

$$\begin{aligned} \left|\frac{5}{2}\right\rangle &= \sqrt{\frac{6}{7}} \left|3, -\frac{1}{2}\right\rangle - \sqrt{\frac{1}{7}} \left|2, \frac{1}{2}\right\rangle, & \left|-\frac{5}{2}\right\rangle &= -\sqrt{\frac{6}{7}} \left|-3, \frac{1}{2}\right\rangle + \sqrt{\frac{1}{7}} \left|-2, -\frac{1}{2}\right\rangle, \\ \left|\frac{3}{2}\right\rangle &= \sqrt{\frac{5}{7}} \left|2, -\frac{1}{2}\right\rangle - \sqrt{\frac{2}{7}} \left|1, \frac{1}{2}\right\rangle, & \left|-\frac{3}{2}\right\rangle &= -\sqrt{\frac{5}{7}} \left|-2, \frac{1}{2}\right\rangle + \sqrt{\frac{2}{7}} \left|-1, -\frac{1}{2}\right\rangle, \\ \left|\frac{1}{2}\right\rangle &= \sqrt{\frac{4}{7}} \left|1, -\frac{1}{2}\right\rangle - \sqrt{\frac{3}{7}} \left|0, \frac{1}{2}\right\rangle, & \left|-\frac{1}{2}\right\rangle &= -\sqrt{\frac{4}{7}} \left|-1, \frac{1}{2}\right\rangle + \sqrt{\frac{3}{7}} \left|0, -\frac{1}{2}\right\rangle. \end{aligned} \quad (\text{S2})$$

Using the above Γ_8 quartet and two $5d$ orbitals of e_g symmetry (d_{z^2} and $d_{x^2-y^2}$), we first derive the spin-orbital structure of the hopping integrals between these states up to second nearest-neighbour bonds. This is done following the Slater-Koster tables for the f and d orbitals [4, 5]. Then we transform the Hamiltonian into the momentum space, and represent it in the following matrix form, written in the basis of the $\{\alpha_+, \alpha_-, \beta_+, \beta_-, d_{z^2\uparrow}, d_{z^2\downarrow}, d_{x^2-y^2\uparrow}, d_{x^2-y^2\downarrow}\}$ states:

$$\mathcal{H} = \begin{bmatrix} E_f I + H_{ff} & H_{df} \\ H_{df}^* & E_d I + H_{dd} \end{bmatrix}. \quad (\text{S3})$$

Here, E_f and E_d are the on-site energies for f and d orbitals, and I is the 4×4 unit matrix. The 4×4 block matrices $H_{ff} = H_{ff1} + H_{ff2}$ and $H_{dd} = H_{dd1} + H_{dd2}$ are the kinetic energies for f and d electrons, respectively, with the subscripts 1 and 2 representing the nearest-neighbor (NN) and the next-nearest-neighbor (NNN) bonds; the 4×4 matrix $H_{df} = H_{df1} + H_{df2}$ denotes the hybridization between d and f orbitals. The explicit forms of these submatrices are introduced term by term below.

The NN hopping energy H_{ff1} for the Γ_8 states $\{\alpha_+, \alpha_-, \beta_+, \beta_-\}$ reads as:

$$H_{ff1} = \begin{bmatrix} t_{f1}\phi_1(\mathbf{k}) + t'_{f1}\phi_2(\mathbf{k}) & 0 & (t_{f1} - t'_{f1})\phi_3(\mathbf{k}) & 0 \\ 0 & t_{f1}\phi_1(\mathbf{k}) + t'_{f1}\phi_2(\mathbf{k}) & 0 & (t_{f1} - t'_{f1})\phi_3(\mathbf{k}) \\ (t_{f1} - t'_{f1})\phi_3(\mathbf{k}) & 0 & t_{f1}\phi_2(\mathbf{k}) + t'_{f1}\phi_1(\mathbf{k}) & 0 \\ 0 & (t_{f1} - t'_{f1})\phi_3(\mathbf{k}) & 0 & t_{f1}\phi_2(\mathbf{k}) + t'_{f1}\phi_1(\mathbf{k}) \end{bmatrix}, \quad (\text{S4})$$

where t_{f1} (t'_{f1}) is an effective, i.e., rescaled by the coefficients of fractional parentage [2], hopping between α - α (β - β) orbitals along the z -axis. The real functions ϕ_i are given by: $\phi_1(\mathbf{k}) = c_x + c_y + 4c_z$, $\phi_2(\mathbf{k}) = 3(c_x + c_y)$, and $\phi_3(\mathbf{k}) = \sqrt{3}(c_y - c_x)$, with $c_j = \cos k_j$ ($j = x, y, z$).

For the NNN hopping terms between the f orbitals, we have

$$H_{ff2} = \begin{bmatrix} t_{f2}\phi_4(\mathbf{k}) + t'_{f2}\phi_5(\mathbf{k}) & 0 & (t_{f2} - t'_{f2})\phi_6(\mathbf{k}) + it'_{f2}\phi_7(\mathbf{k}) & t'_{f2}\phi_8(\mathbf{k}) \\ 0 & t_{f2}\phi_4(\mathbf{k}) + t'_{f2}\phi_5(\mathbf{k}) & -t'_{f2}\phi_8(\mathbf{k}) & (t_{f2} - t'_{f2})\phi_6(\mathbf{k}) - it'_{f2}\phi_7(\mathbf{k}) \\ (t_{f2} - t'_{f2})\phi_6(\mathbf{k}) - it'_{f2}\phi_7(\mathbf{k}) & -t'_{f2}\phi_8(\mathbf{k}) & t_{f2}\phi_5(\mathbf{k}) + t'_{f2}\phi_4(\mathbf{k}) & 0 \\ t'_{f2}\phi_8^*(\mathbf{k}) & (t_{f2} - t'_{f2})\phi_6(\mathbf{k}) + it'_{f2}\phi_7(\mathbf{k}) & 0 & t_{f2}\phi_5(\mathbf{k}) + t'_{f2}\phi_4(\mathbf{k}) \end{bmatrix}. \quad (\text{S5})$$

Here, $\phi_4(\mathbf{k}) = c_x c_z + c_y c_z + 4c_x c_y$, $\phi_5(\mathbf{k}) = 3c_z(c_x + c_y)$, $\phi_6(\mathbf{k}) = \sqrt{3}(c_x - c_y)c_z$, $\phi_7(\mathbf{k}) = 4s_x s_y$, $\phi_8(\mathbf{k}) = 4(s_x + i s_y)s_z$, and $s_j = \sin k_j$ ($j = x, y, z$). t_{f2} (t'_{f2} , t''_{f2}) is the effective hopping amplitude between in-plane NNN α - α (β - β , α - β) orbitals.

Correspondingly, the matrix forms for NN hopping H_{dd1} and NNN hopping H_{dd2} between d orbitals, written in the $\{d_{z^2\uparrow}, d_{z^2\downarrow}, d_{x^2-y^2\uparrow}, d_{x^2-y^2\downarrow}\}$ basis, with \uparrow, \downarrow representing the up and down spin states, are:

$$H_{dd1} = \begin{bmatrix} t_{d1}\phi_1(\mathbf{k}) + t'_{d1}\phi_2(\mathbf{k}) & 0 & (t_{d1} - t'_{d1})\phi_3(\mathbf{k}) & 0 \\ 0 & t_{d1}\phi_1(\mathbf{k}) + t'_{d1}\phi_2(\mathbf{k}) & 0 & (t_{d1} - t'_{d1})\phi_3(\mathbf{k}) \\ (t_{d1} - t'_{d1})\phi_3(\mathbf{k}) & 0 & t_{d1}\phi_2(\mathbf{k}) + t'_{d1}\phi_1(\mathbf{k}) & 0 \\ 0 & (t_{d1} - t'_{d1})\phi_3(\mathbf{k}) & 0 & t_{d1}\phi_2(\mathbf{k}) + t'_{d1}\phi_1(\mathbf{k}) \end{bmatrix}, \quad (\text{S6})$$

and

$$H_{dd2} = \begin{bmatrix} t_{d2}\phi_4(\mathbf{k}) + t'_{d2}\phi_5(\mathbf{k}) & 0 & (t_{d2} - t'_{d2})\phi_6(\mathbf{k}) & 0 \\ 0 & t_{d2}\phi_4(\mathbf{k}) + t'_{d2}\phi_5(\mathbf{k}) & 0 & (t_{d2} - t'_{d2})\phi_6(\mathbf{k}) \\ (t_{d2} - t'_{d2})\phi_6(\mathbf{k}) & 0 & t_{d2}\phi_5(\mathbf{k}) + t'_{d2}\phi_4(\mathbf{k}) & 0 \\ 0 & (t_{d2} - t'_{d2})\phi_6(\mathbf{k}) & 0 & t_{d2}\phi_5(\mathbf{k}) + t'_{d2}\phi_4(\mathbf{k}) \end{bmatrix}. \quad (\text{S7})$$

The NN hybridization term H_{df1} between d - and f -states reads as:

$$H_{df1} = i \begin{bmatrix} V_1\phi_9(\mathbf{k}) & -(V_1 + 3V'_1)\phi_{10}(\mathbf{k}) & 0 & \sqrt{3}(V_1 - V'_1)\phi_{10}^*(\mathbf{k}) \\ -(V_1 + 3V'_1)\phi_{10}^*(\mathbf{k}) & -V_1\phi_9(\mathbf{k}) & \sqrt{3}(V_1 - V'_1)\phi_{10}(\mathbf{k}) & 0 \\ 0 & \sqrt{3}(V_1 - V'_1)\phi_{10}^*(\mathbf{k}) & V'_1\phi_9(\mathbf{k}) & -(3V_1 + V'_1)\phi_{10}(\mathbf{k}) \\ \sqrt{3}(V_1 - V'_1)\phi_{10}(\mathbf{k}) & 0 & -(3V_1 + V'_1)\phi_{10}^*(\mathbf{k}) & -V'_1\phi_9(\mathbf{k}) \end{bmatrix}, \quad (\text{S8})$$

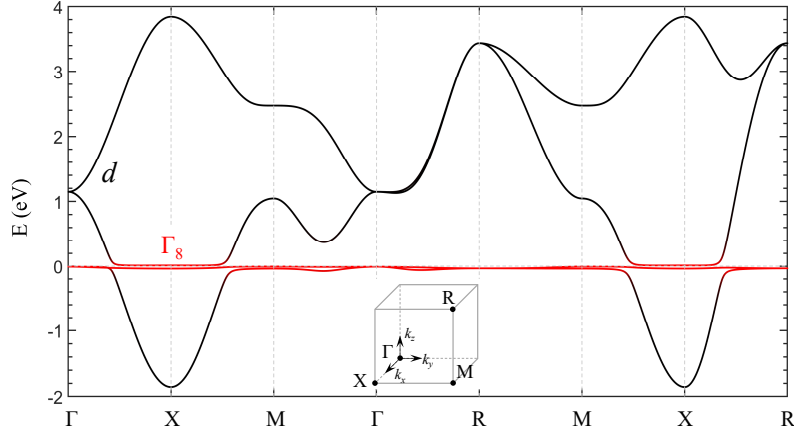


FIG. S2: Band structure along high-symmetry paths in the Brillouin zone, calculated with the parameters given in Eq. (S10). Black and red colors are for d - and f -like band states.

where V_1 (V'_1) represents an effective hybridization amplitude between α - d_{z^2} (β - $d_{x^2-y^2}$) orbitals, $\phi_9(\mathbf{k}) = -4s_z$ and $\phi_{10}(\mathbf{k}) = s_x - is_y$.

Finally, the NNN hybridization Hamiltonian H_{df2} is:

$$H_{df2} = i \begin{bmatrix} [V_2 + 3V'_2 - \sqrt{3}(V_2'' + V_2''')] \phi_{11}(\mathbf{k}) & V_2 \phi_{13}(\mathbf{k}) + [V_2 + 3V'_2 + \sqrt{3}(V_2'' + V_2''')] \phi_{14}(\mathbf{k}) \\ V_2 \phi_{13}^*(\mathbf{k}) + [V_2 + 3V'_2 + \sqrt{3}(V_2'' + V_2''')] \phi_{14}^*(\mathbf{k}) & -[V_2 + 3V'_2 - \sqrt{3}(V_2'' + V_2''')] \phi_{11}(\mathbf{k}) \\ [\sqrt{3}(V_2 - V'_2) - 3V_2'' + V_2'''] \phi_{12}(\mathbf{k}) & V_2'' \phi_{13}^*(\mathbf{k}) + [\sqrt{3}(V_2 - V'_2) + 3V_2'' - V_2'''] \phi_{14}^*(\mathbf{k}) \\ V_2'' \phi_{13}(\mathbf{k}) + [\sqrt{3}(V_2 - V'_2) + 3V_2'' - V_2'''] \phi_{14}(\mathbf{k}) & -[\sqrt{3}(V_2 - V'_2) - 3V_2'' + V_2'''] \phi_{12}(\mathbf{k}) \end{bmatrix}, \quad (S9)$$

$$\begin{bmatrix} [\sqrt{3}(V_2 - V'_2) + V_2'' - 3V_2'''] \phi_{12}(\mathbf{k}) & V_2'' \phi_{13}^*(\mathbf{k}) + [\sqrt{3}(V_2 - V'_2) - V_2'' + 3V_2'''] \phi_{14}^*(\mathbf{k}) \\ V_2'' \phi_{13}(\mathbf{k}) + [\sqrt{3}(V_2 - V'_2) - V_2'' + 3V_2'''] \phi_{14}(\mathbf{k}) & -[\sqrt{3}(V_2 - V'_2) + V_2'' - 3V_2'''] \phi_{12}(\mathbf{k}) \\ [3V_2 + V'_2 + \sqrt{3}(V_2'' + V_2''')] \phi_{11}(\mathbf{k}) & V_2 \phi_{13}(\mathbf{k}) + [3V_2 + V'_2 - \sqrt{3}(V_2'' + V_2''')] \phi_{14}(\mathbf{k}) \\ V_2' \phi_{13}^*(\mathbf{k}) + [3V_2 + V'_2 - \sqrt{3}(V_2'' + V_2''')] \phi_{14}^*(\mathbf{k}) & -[3V_2 + V'_2 + \sqrt{3}(V_2'' + V_2''')] \phi_{11}(\mathbf{k}) \end{bmatrix}, \quad (S9)$$

where V_2 (V'_2 , V_2'' , V_2''') is the hybridization between in-plane NNN α - d_{z^2} (β - $d_{x^2-y^2}$, α - $d_{x^2-y^2}$, β - d_{z^2}) orbitals, and $\phi_{11}(\mathbf{k}) = s_z(c_x + c_y)$, $\phi_{12}(\mathbf{k}) = s_z(c_x - c_y)$, $\phi_{13}(\mathbf{k}) = 4(s_x c_y - ic_x s_y)$, and $\phi_{14}(\mathbf{k}) = c_z(s_x - is_y)$. We note that the spin-orbital structure of the hopping Hamiltonians obtained above is consistent with the previous works [6, 7].

For the valence state with $v = 2.56$, i.e., at ambient pressure, we use the following parameter set:

$$\begin{aligned} E_d &= 1.6 \text{ eV}, & E_f &= -0.02 \text{ eV}, \\ t_{d1} &= -0.32 \text{ eV}, & t'_{d1} &= -0.4t_{d1}, & t_{d2} &= -0.6t_{d1}, & t'_{d2} &= -0.4t_{d2}, \\ t_{f1} &= 0.0036 \text{ eV}, & t'_{f1} &= -0.4t_{f1}, & t_{f2} &= -0.2t_{f1}, & t'_{f2} &= -0.4t_{f2}, & t''_{f2} &= 0.4t_{f2}, \\ V_1 &= 0.036 \text{ eV}, & V'_1 &= -0.4V_1, & V_2 &= 0.1V_1, & V'_2 &= -0.2V_2, & V_2'' &= -0.2V_2, & V_2''' &= 0.1V_2. \end{aligned} \quad (S10)$$

The resulting band structure is shown in Fig. S2. The $4f$ -dominated bands are located around the Fermi level, while the $5d$ -like states disperse widely from -2 eV to 4 eV. A hybridization gap of $\simeq 17$ meV is consistent with the ARPES data [8].

SIII. Magnetic susceptibility and spin exciton mode

The bare magnetic susceptibility $\chi_0(\mathbf{q}, \omega)$ in Eq. (3) of the main text is evaluated as follows:

$$\chi_0(\mathbf{q}, \omega) = \sum_{klm} \frac{| \langle l_{\mathbf{k}} | J_z | m_{\mathbf{k}+\mathbf{q}} \rangle |^2}{\omega + E_{l,\mathbf{k}} - E_{m,\mathbf{k}+\mathbf{q}} + i0^+} (f_{E_{m,\mathbf{k}+\mathbf{q}}} - f_{E_{l,\mathbf{k}}}). \quad (S11)$$

Here, l and m run over the eight bands derived from the Γ_8 and $d(e_g)$ states, as discussed in the previous section. Momentum \mathbf{k} runs over the first Brillouin zone. The z component of the angular momentum $J = 5/2$, projected onto

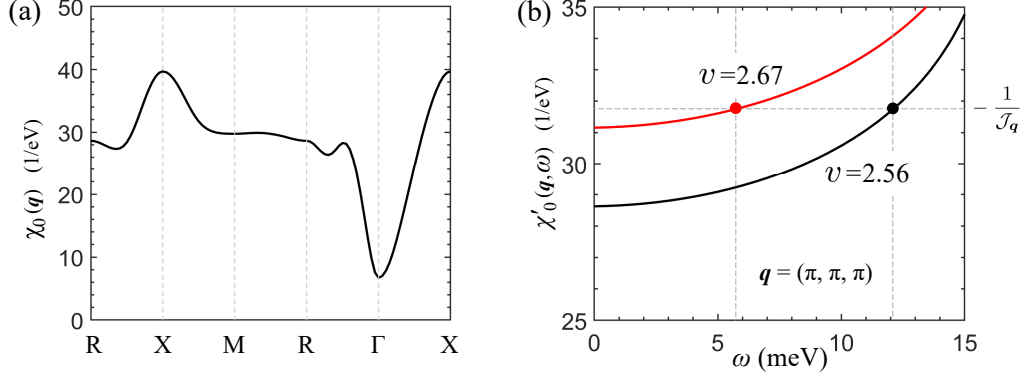


FIG. S3: (a) Static magnetic susceptibility $\chi_0(\mathbf{q}, 0)$ at valence $v = 2.56$. (b) Frequency dependence of the real part of the bare magnetic susceptibility $\chi'_0(\mathbf{q}, \omega)$ for R-point with $\mathbf{q} = (\pi, \pi, \pi)$, at valence $v = 2.56$ (black) and $v = 2.67$ (red). Black and red dots determine the corresponding spin-exciton energies $\omega_{\mathbf{q}}$ following from Eq. (S14). The exchange couplings $(\mathcal{J}_1, \mathcal{J}_2, \mathcal{J}_3) = (14.7, 6.5, 2.7)$ meV are used as in the main text. Note that $\omega_{\mathbf{q}}$ is reduced by a factor of two as the Sm valence v is slightly increased.

the Γ_8 quartet, is given by $J_z = s_\alpha^z + \frac{11}{3}s_\beta^z$, where the pseudospins one-half s_α and s_β operate within the α and β Kramers doublets defined in Eq. (S1) above.

Figure S3(a) shows the static susceptibility $\chi_0(\mathbf{q})$ for $v = 2.56$, calculated using the parameter set of Eq. (S10). Its momentum dependence is decided by the heavy-band dispersions of Γ_8 character, and has a maximum at the X-point with $\mathbf{q} = (\pi, 0, 0)$. However, the exchange couplings between the Γ_8 states must be considered to obtain the full momentum and energy dependence of the magnetic response. Within the random phase approximation, one finds

$$\chi(\mathbf{q}, \omega) = \frac{\chi_0(\mathbf{q}, \omega)}{1 + \mathcal{J}_{\mathbf{q}}\chi_0(\mathbf{q}, \omega)}. \quad (\text{S12})$$

Including the exchange couplings \mathcal{J}_R up to third-nearest neighbours, we obtain

$$\mathcal{J}_{\mathbf{q}} = 2\mathcal{J}_1(c_x + c_y + c_z) + 4\mathcal{J}_2(c_x c_y + c_y c_z + c_z c_x) + 8\mathcal{J}_3 c_x c_y c_z, \quad (\text{S13})$$

where $c_j = \cos q_j$ ($j = x, y, z$). In addition to particle-hole excitations from $\chi_0(\mathbf{q}, \omega)$, Eq. (S12) contains a pole at energy $\omega_{\mathbf{q}}$, which satisfies the following equation:

$$\chi'_0(\mathbf{q}, \omega_{\mathbf{q}}) = -\frac{1}{\mathcal{J}_{\mathbf{q}}}. \quad (\text{S14})$$

The spectral weight $A_{\mathbf{q}}$ of this collective (“spin-exciton”) mode can be obtained by expanding Eq. (S12) near the pole. It is proportional to the inverse of the derivative of the real part of bare susceptibility at the peak position $\omega_{\mathbf{q}}$:

$$A_{\mathbf{q}} = \frac{1}{\mathcal{J}_{\mathbf{q}}^2} \left(\frac{d\chi'_0(\mathbf{q}, \omega)}{d\omega} \right)_{\omega=\omega_{\mathbf{q}}}^{-1}. \quad (\text{S15})$$

As illustrated in Fig. S3(b), the susceptibility $\chi'_0(\mathbf{q}, \omega)$ increases with the valence v , resulting in a strong softening of the spin-exciton energy. Consequently, the spin-exciton peak gains a large intensity, see Fig. 2(a) of the main text.

A comment is in order concerning the spin susceptibility calculations. It is essential to use a realistic Γ_8 quartet model, because it contains an additional flat band near the Fermi level, in comparison with a simple f -doublet model often used in the literature. Our Γ_8 quartet model calculations, however, still underestimate the $\chi_0(\mathbf{q}, \omega)$ values, because we neglected transitions to the Γ_7 and higher levels. While the corresponding Van Vleck-type contributions would not affect the momentum dependences of $\chi_0(\mathbf{q}, \omega)$, thus not changing the qualitative picture, the exchange parameter values \mathcal{J}_R , required to generate the spin-exciton peak positions consistent with the experimental data, will decrease accordingly.

In the magnetic phases, we treat the exchange interactions in Eq. (2) of the main text in a standard molecular field approximation, and calculate the mean-field value of $\langle J_z \rangle$ in a self-consistent way. The ordered magnetic moment M , shown in Fig. 2(b) of the main text, is defined as $M = g_J \langle J_z \rangle$, with the g -factor of $g_J = 2/7$.

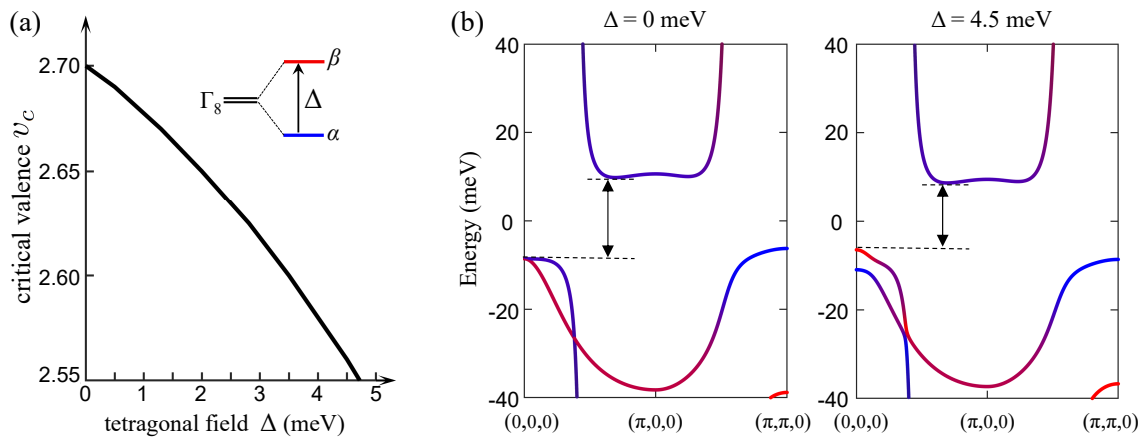


FIG. S4: (a) Critical valence v_c for magnetic ordering in SmB_6 as a function of tetragonal crystal field, which splits the Γ_8 quartet into α and β doublets by Δ (inset). (b) Band structure for the valence state with $v = 2.56$ (corresponding to ambient pressure), calculated at different Δ values. The blue and red colors indicate the contributions from the α and β doublets, respectively. Tetragonal splitting reduces the band gaps as indicated by double arrows.

SIII. Tetragonal crystal field effect on the phase transition

SmB_6 becomes magnetically ordered metal when the exchange field is strong enough to overcome the hybridization gap. This is realized under pressure, which increases the Sm valence hence the density of magnetoactive Sm^{3+} ions. The present Γ_8 quartet model suggests that there is an alternative way to stabilize magnetic order even at ambient pressure, by reducing the cubic symmetry to tetragonal one, that is, by splitting Γ_8 quartet into the α and β doublet states. In practice, such a tetragonal crystal field is induced by an external strain. It is important to notice, however, that cubic symmetry is actually broken at the surface of crystal even without any strain, and also near the defects in the bulk, so the tetragonal field effect considered here is generic and essential to understand the precise structure of the surface and defect states in mixed-valence compounds of cubic symmetry such as SmB_6 .

To substantiate the above physical picture, we have calculated the critical valence v_c , at which the magnetic order and concomitant metal-insulator transition should appear in SmB_6 , by including the tetragonal crystal field Hamiltonian $\Delta(n_\beta - n_\alpha)/2$. The result shown in Fig. S4(a) tells that the tetragonal splitting as small as $\Delta \simeq 4.5$ meV is sufficient to reduce the critical v_c to 2.56, i.e., to the Sm valence in SmB_6 at ambient pressure, thus driving this mixed-valence compound into a magnetically ordered state. The origin of this effect is simple and explained in Fig. S4(b). Namely, splitting of the Γ_8 quartet modifies the band structure near the Fermi level and reduces the hybridization gap. This enhances the magnetic response, given by Eqs. (S11) and (S12), resulting in the spin-exciton softening and magnetic order. Physically, strong impact of the tetragonal field is due to the proximity of SmB_6 to a magnetic order, which can be controlled by strain and/or uniaxial pressure as suggested by our work. In fact, the tetragonal distortion which supports magnetic order is naturally present at the surface of crystal. We believe that this provides a natural explanation for the surface magnetism observed in SmB_6 at ambient pressure [9, 10].

SIV. Topological invariants for materials with glide mirror symmetries

For the paramagnetic as well as the antiferromagnetic phases of SmB_6 the combination of inversion symmetry P with time-reversal symmetry (with the operators T , T_A , and T_G , respectively) leads by Kramers theorem to twofold degenerate bands. Note that despite the translations included in T_A and T_G the prerequisite $(PT_A)^2 = (PT_G)^2 = -1$ of the Kramers theorem holds. Due to the degeneracy for each electronic band, one can freely choose a basis of the corresponding two-dimensional eigenspace of the Hamiltonian. To describe the topology of gapped subsystems, besides using the conventional \mathbb{Z}_2 invariant [11], it is possible to resolve the internal structure of the degenerate bands by considering eigenspaces of the crystalline symmetries. One example of this is the mirror Chern number, which refines the \mathbb{Z}_2 invariant [12]. Hereby, one considers a mirror plane in reciprocal space, where the Hamiltonian is completely gapped. Using the mirror symmetry one may block-diagonalize the Hamiltonian into two blocks, one for each mirror eigenvalue. Each matrix block is found to exhibit a non-zero Chern number, whereas the total Chern number vanishes due to time-reversal symmetry (or the corresponding anti-unitary symmetry of an antiferromagnet).

A non-zero mirror Chern number is defined as the difference between the Chern numbers of the two matrix blocks.

In order to describe the topology of nodal lines, which are gapless features unlike the previously discussed gapped systems, one might try to define a mirror Berry phase in an analogous fashion [13]. However, it turns out that this is not a viable approach for the A-type antiferromagnetic phase of SmB₆. The reason is that in the A-type antiferromagnetic phase the available mirror symmetries are *nonsymmorphic*, e.g., \tilde{m}_x is a glide mirror symmetry, since it comprises a translation $t(0, 0, 1)$ along the z direction. As a result the projection into a \tilde{m}_x symmetry eigenspace leads to a block-diagonal Hamiltonian that is not periodic in the Brillouin zone anymore. Instead, at $k_z = -\pi/2$ the eigenstates of each block become pairwise orthogonal to those at $k_z = +\pi/2$. To see this, consider the glide mirror eigenvalues $\{\pm ie^{ik_z}\}$ of \tilde{m}_x , which exchange over the course of the Brillouin zone. Note that we describe the Brillouin zone of the doubled magnetic unit cell with the original lattice constants, hence the Brillouin zone extends over the interval $k_z \in [-\pi/2, \pi/2]$ for the A-type antiferromagnetic phase. The exchange of mirror eigenvalues is independent of the unit cell convention and makes it impossible to consider a mirror Berry phase or, more generally, a Wilson loop in a single mirror subspace. Nevertheless, we will show below that a *mirror-graded* Wilson loop over twice the length of the Brillouin zone captures the band topology.

A non-Abelian Berry connection is needed to treat a system with degenerate bands [14]. Hence, we consider the non-Abelian Wilson loop in a tight-binding formulation [15]

$$[\mathcal{W}(\mathcal{L})]^{mn} = \langle U_{\mathbf{k}^{(0)}+\mathbf{G}}^m | W(\mathbf{k}^{(0)} + \mathbf{G} \leftarrow \mathbf{k}^{(0)}) | U_{\mathbf{k}^{(0)}}^n \rangle, \quad (\text{S16})$$

$$W(k^{(\gamma)} \leftarrow k^{(\beta)}) = \prod_{\alpha}^{k^{(\gamma)} \leftarrow k^{(\beta)}} \mathcal{P}_{\mathbf{k}^{(\alpha)}}^{\text{occ}}, \quad (\text{S17})$$

$$\mathcal{P}_{\mathbf{k}}^{\text{occ}} = \sum_{i=1}^{n_{\text{occ}}} |U_{\mathbf{k}}^i\rangle \langle U_{\mathbf{k}}^i|, \quad (\text{S18})$$

where \mathbf{G} is the reciprocal lattice vector that relates two equivalent starting points \mathbf{k}_0 . The Wilson matrix $W(\mathcal{L})$, Eq. (S16), is given by the product of the projectors $\mathcal{P}_{\mathbf{k}}^{\text{occ}}$ on the n_{occ} occupied eigenstates $|U_{\mathbf{k}}^i\rangle$ of the Hamiltonian along a closed loop \mathcal{L} . The k -points along the Wilson loop \mathcal{L} are $\{\mathbf{k}^{(0)} + \mathbf{G}, \mathbf{k}^{(N)}, \mathbf{k}^{(N-1)}, \dots, \mathbf{k}^{(0)}\}$ with $N > 1$, where a periodic gauge is assumed, i.e., $|U_{\mathbf{k}^{(0)}+\mathbf{G}}^n\rangle = |U_{\mathbf{k}^{(0)}}^n\rangle$. For an arbitrary, not necessarily closed, segment of the loop \mathcal{L} we denote the corresponding tight-binding Wilson matrix by $W(k^{(\gamma)} \leftarrow k^{(\beta)})$. While the eigenspectra of the continuum Wilson loop and the tight-binding Wilson loop matrix, Eq. (S16), may differ, they coincide in their real eigenvalues, and in their complex eigenvalues up to a phase [15]. This turns out to be sufficient to qualitatively capture the flow of the Wilson loop spectrum as a function of \mathbf{k}^0 , which in turn characterizes the topology of the surface bands [16].

The bulk-boundary correspondence that relates surface bands to the bulk topology [16] requires the use of the cell-periodic basis convention as introduced in Ref. [17]. In the paramagnetic phase, Eq. (S3), the convention plays no role, because there is only one site per unit cell, whereas in the antiferromagnetic phases there are two lattice sites per unit cell. For the latter the cell-periodic convention corresponds to a Fourier transform using the real atomic positions, instead of the coordinates of the unit cell. In this convention the surface spectrum can be continuously deformed to the Wilson loop spectrum [16]. Here, we only argue for the existence of surface states from the bulk-boundary correspondence, while quantitative statements on the shape of surface states rely on direct calculations, cf. Fig. 3 in the main text.

We implemented the Wilson loop matrix $\mathcal{W}(\mathcal{L}_{k_y})$ according to Eq. (S16) for loops \mathcal{L}_{k_y} parametrized by (π, k_y, k_z) for $k_z \in [-\pi/2, \pi/2]$, i.e., $\mathbf{k}^{(0)} = (\pi, k_y, -\pi/2)$ and $\mathbf{G} = (0, 0, \pi)$, and at all even-integer fillings up to the Fermi energy. To describe the flow of the Wilson loop spectrum as a function of k_y , one considers the complex phases $\theta(k_y)$ of the eigenvalues of the Wilson loop matrix $\mathcal{W}(\mathcal{L}_{k_y})$, see Fig. S5(a). We find that these complex phases reach all possible values, i.e., $-\pi$ to $+\pi$, within the Brillouin zone, which due to their relation to the Wannier charge centers implies the presence of surface states, see Fig. S5(a,b) [16]. Additionally, in this geometry signatures of the Dirac nodal lines are expected, once k_y is close to the position of the nodal lines. Indeed, we find jumps in $\theta(k_y)$ once the loop \mathcal{L}_{k_y} passes through one of the nodal lines. Yet, this approach is not optimal to capture the topology of Dirac nodal lines. The fourfold degenerate Dirac nodal lines exhibit twice the Berry phase that a twofold degenerate nodal line carries. In other words, the Berry phase, which is the total of all $\theta(k_y)$ for loops enclosing the nodal line, is trivial. Thus, we propose in the following a mirror-graded Wilson loop, which makes the topological quantization evident.

To refine the concept of non-Abelian Wilson loops, we use the glide mirror symmetry \tilde{m}_x to block-diagonalize the Hamiltonian before we define the mirror-graded Wilson loop. We project the Hamiltonian into the occupied subspace belonging to the mirror eigenvalue $+ie^{ik_z}$ of \tilde{m}_x with the corresponding projector $\mathcal{P}_{\mathbf{k}}^+$ and obtain $H^+(\mathbf{k}) = \mathcal{P}_{\mathbf{k}}^+ H(\mathbf{k}) \mathcal{P}_{\mathbf{k}}^+$. The eigenvalues $\{\pm ie^{ik_z}\}$ of \tilde{m}_x exchange over the course of the Brillouin zone, which implies the eigenspace belonging to the eigenvalue $+ie^{ik_z}$ at $k_z = \pi/2$ has no overlap with the same eigenspace at $k_z = -\pi/2$, whereas the eigenspaces

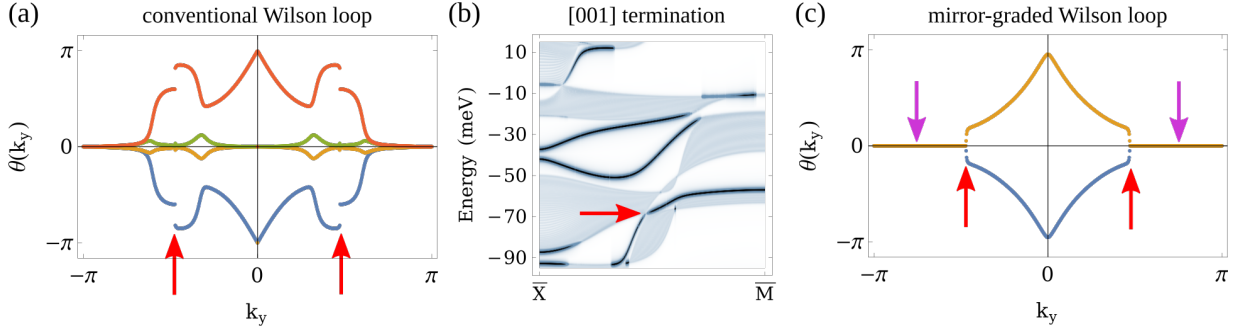


FIG. S5: Comparison of Wilson loop spectra for the A-type antiferromagnetic phase. All loops \mathcal{L}_{k_y} are taken at constant $k_x = \pi$ and along the k_z axis. The red arrows highlight the positions where k_y cuts a Dirac nodal line. (a) Spectrum of the Wilson loop calculated according to Eq. (S16) at two filled, degenerate bands. (b) Corresponding band structure of a slab in [001] termination with highlighted surface states, see also Fig. 3 in the main text. (c) Spectrum of the mirror-graded Wilson loop calculated according to Eq. (S19) for two filled bands, where the number of different values of $\theta(k_y)$ at each k_y is half of that in (a), due to the projection on one eigenspace of the glide mirror symmetry \tilde{m}_x in Eq. (S19). Purple arrows mark the regions where $\theta(k_y)$ has an exact degeneracy and a flat dispersion with $\theta(k_y) \equiv 0$.

at $k_z = +\pi$ and $k_z = -\pi$ are isomorphic. Thus, we propose to extend the loop \mathcal{L} from the interval $k_z \in [-\pi/2, \pi/2]$ to $k_z \in [-\pi, \pi]$. Analogously to Eq. (S16) we then define a mirror-graded Wilson loop \mathcal{W}^+ using the eigenstates $|U_{\mathbf{k}}^{+,i}\rangle$ of $H^+(\mathbf{k})$,

$$[\mathcal{W}^+(\mathcal{L})]^{mn} = \left\langle U_{\mathbf{k}^{(0)+2\mathbf{G}}}^{+,m} \left| W^+(\mathbf{k}^{(0)} + 2\mathbf{G} \leftarrow \mathbf{k}^{(0)}) \right| U_{\mathbf{k}^{(0)}}^{+,n} \right\rangle, \quad (\text{S19})$$

$$W^+(\mathbf{k}^{(\gamma)} \leftarrow \mathbf{k}^{(\beta)}) = \prod_{\alpha}^{k^{(\gamma)} \leftarrow k^{(\beta)}} \mathcal{P}_{\mathbf{k}^{(\alpha)}}^{+, \text{occ}}, \quad (\text{S20})$$

$$\mathcal{P}_{\mathbf{k}}^{+, \text{occ}} = \sum_{i=1}^{n_{\text{occ}}} |U_{\mathbf{k}}^{+,i}\rangle \langle U_{\mathbf{k}}^{+,i}|, \quad (\text{S21})$$

where $\mathcal{P}_{\mathbf{k}}^{+, \text{occ}}$ projects onto occupied eigenstates of $H(\mathbf{k})$ with mirror eigenvalue $+ie^{ik_z}$. The reciprocal lattice vector to close the loop is now $2\mathbf{G}$, i.e., for the A-type antiferromagnetic order $2\mathbf{G} = (0, 0, 2\pi)$ in units of the inverse lattice constant of SmB_6 . We are going to argue that Eq. (S19) is not missing terms appearing in Eq. (S16). Yet, since the order in which the factors are considered differs between Eqs. (S16) and (S19), the spectrum of the mirror-graded Wilson loop is different. First, note that in the cell-periodic basis convention the representation of the mirror symmetry comprises a k -independent matrix and a k -dependent prefactor. As a result all eigenstates of \tilde{m}_x are constant, which implies in turn that the mirror eigenstates of different eigenvalues at $\mathbf{k}^{(\alpha+1)}$ and $\mathbf{k}^{(\alpha)}$ are pair-wise orthogonal. This allows us to simplify the overlap terms, which occur in the conventional tight-binding Wilson loop, Eq. (S16), in the form of $\langle U_{\mathbf{k}^{(\alpha+1)}}^i | U_{\mathbf{k}^{(\alpha)}}^j \rangle$ for occupied states i and j . This overlap $\langle U_{\mathbf{k}^{(\alpha+1)}}^i | U_{\mathbf{k}^{(\alpha)}}^j \rangle$ is only non-zero within each mirror subspace and therefore the projection $\mathcal{P}_{\mathbf{k}}^+$ does not remove any non-vanishing terms in the Wilson loop. But, as mentioned before, the glide-mirror operator eigenvalues exchange and we cannot meaningfully close our Wilson loop at $k_z = \pi/2$. In other words, the Hamiltonian $H^+(\mathbf{k})$ projected on the eigenspace of $+ie^{ik_z}$ evolves into the Hamiltonian $H^-(\mathbf{k})$ projected on the eigenspace of $-ie^{ik_z}$, i.e., $H^+(\mathbf{k} + (0, 0, \pi)) = H^-(\mathbf{k})$. In conclusion, Eq. (S19) captures both eigenspaces of \tilde{m}_x , as does Eq. (S16), but the mirror-graded Wilson loop does so not simultaneously but consecutively in a longer loop. This leads to Wilson loop matrices $\mathcal{W}^+(\mathcal{L})$ with half the number of rows and columns for the same number of occupied bands.

The mirror-graded Wilson loop, as introduced in Eq. (S19), remedies the issues of the conventional Wilson loop defined in Eq. (S16). We use the new definition and find the Wilson loop spectrum shown in Fig. S5(c). A rapid change in the spectrum of the mirror-graded Wilson loop occurs at the position of the nodal line. It appears that in the vicinity of the Dirac nodal line there is a slope that is too steep for the chosen resolution but not a discontinuity as it is seen in Fig. S5(a). Notably, at the k_y value where the band structure exhibits a nodal line, the mirror-graded Wilson loop $\theta(k_y)$ has a kink, (red arrow) which separates a dispersive region from a nondispersive flat region (pink arrows). We will discuss the reason for this behavior in more detail below. Furthermore, the presence of small avoided crossings in the band structure does not lead to unphysical jumps in the mirror-graded Wilson loop spectrum. Finally,

as far as the plot resolution permits, the Wilson loop spectrum spans the full range of complex phases, see Fig. S5(c), and thus there is still a connection between the Wilson loop and the surface spectrum Fig. S5(b).

To understand the (mirror-graded) Wilson loop spectra, we consider the symmetries that constrain its spectrum. The sum over the band index i of the complex phases $\theta(k_y)_i$ in the Wilson loop $\mathcal{W}(\mathcal{L}_{k_y})$ spectrum corresponds to the usual Berry phase, which in the present case is identically zero due to inversion and time-reversal symmetry [15]. An inversion sends $k_y \rightarrow -k_y$ and inverts the direction of the Wilson loop, which implies that the phase fulfills $\theta(k_y)_i = -\theta(-k_y)_j$ for one pair i and j of band indices. The application of the time reversal operator does not only invert the vector \mathbf{k} but also adds a complex conjugation, which leads to $\theta(k_y)_i = \theta(-k_y)_i$. Together inversion and time reversal imply a symmetric spectrum around $\theta = 0$ with $\theta(k_y)_i = -\theta(k_y)_j$ and thus a vanishing Berry phase.

After this preliminary discussion of symmetries we can return to the question, why there are flat bands in the spectrum of the mirror-graded Wilson loop in Fig. S5(c). We are going to connect the Dirac nodal lines, which are protected by a second mirror symmetry, namely the symmorphic operation m_z , and show under which circumstances the mirror-graded non-Abelian Wilson loop is exactly determined by the mirror eigenvalues $\lambda_{m_z} \in \{\pm i\}$ of m_z . While the latter is generally the case for Wilson loops of non-degenerate bands perpendicular to a mirror plane, for degenerate bands this is not the case, cf. Fig. S5(a). Nevertheless, the mirror-graded non-Abelian Wilson loop partially recovers this connection between the Berry phases $\theta(k_y)_i$ and the mirror eigenvalues λ_{m_z} . The action of m_z on eigenstates $|U_{k_z}^n, \lambda_{\tilde{m}_x}\rangle$ of \tilde{m}_x is given by $m_z |U_{k_z}^n, \lambda_{\tilde{m}_x}\rangle \propto |U_{-k_z}^n, -\lambda_{\tilde{m}_x}\rangle$, where the eigenvalue $\lambda_{\tilde{m}_x}$ denotes the mirror subspace used in the mirror-graded Wilson loop, Eq. (S19). Here, the k_x and k_y dependence is not shown explicitly. By using that the mirror \tilde{m}_x eigenvalues and eigenstates are related due to their k_z dependence, one may rewrite $|U_{-k_z}^n, -\lambda_{\tilde{m}_x}\rangle \propto |U_{\pi-k_z}^n, \lambda_{\tilde{m}_x}\rangle$. Because all appearing proportionality factors have a unit modulus, and thus drop out in the tight-binding Wilson loop, one finds the relation $m_z W(k_z^{(\beta)} \leftarrow k_z^{(\alpha)}) m_z^\dagger = W(\pi - k_z^{(\beta)} \leftarrow \pi - k_z^{(\alpha)})$. To be specific, this can be obtained by introducing $\mathbb{1} = m_z^\dagger m_z$ in each inner product contained in $W(k_z^{(\beta)} \leftarrow k_z^{(\alpha)})$, cf. Eq. (S20). In the following we will split the full mirror-graded Wilson loop into two parts, which then can be related by the relation above, yielding

$$[\mathcal{W}^+(\mathcal{L}_{k_y})]^{mn} = \left\langle U_{-\pi/2}^{+,m} \left| W^+(\frac{3\pi}{2} \leftarrow -\frac{\pi}{2}) \right| U_{\pi/2}^{+,n} \right\rangle = \left\langle U_{-\pi/2}^{+,m} \left| W^+(\frac{3\pi}{2} \leftarrow \frac{\pi}{2}) W^+(\frac{\pi}{2} \leftarrow -\frac{\pi}{2}) \right| U_{\pi/2}^{+,n} \right\rangle \quad (\text{S22})$$

$$= \left\langle U_{-\pi/2}^{+,m} \left| m_z^\dagger W^+(-\frac{\pi}{2} \leftarrow \frac{\pi}{2}) m_z W^+(\frac{\pi}{2} \leftarrow -\frac{\pi}{2}) \right| U_{\pi/2}^{+,n} \right\rangle \quad (\text{S23})$$

$$= \sum_{opq} \left\langle U_{-\pi/2}^{+,m} \left| m_z^\dagger \left| U_{-\pi/2}^{+,o} \right\rangle \left\langle U_{-\pi/2}^{+,o} \right| W^+(-\frac{\pi}{2} \leftarrow \frac{\pi}{2}) \left| U_{\pi/2}^{+,p} \right\rangle \right. \\ \left. \times \left\langle U_{\pi/2}^{+,p} \left| m_z \left| U_{\pi/2}^{+,q} \right\rangle \left\langle U_{\pi/2}^{+,q} \right| W^+(\frac{\pi}{2} \leftarrow -\frac{\pi}{2}) \left| U_{\pi/2}^{+,n} \right\rangle \right. \right\rangle, \quad (\text{S24})$$

where in the last step identity operators have been introduced that can be directly reduced to summations over occupied bands by the projectors in $W^+(\dots)$. In principle the second and fourth term of Eq. (S24) cancel if they are multiplied as matrices. Hence, one finds again the result obtained from inversion and time-reversal symmetry, i.e., $\ln \det \mathcal{W}(\mathcal{L}_{k_y}) = 0$ meaning the Berry phase vanishes. Furthermore, one may now understand the emergence of flat bands in Fig. S5(c). If all occupied bands have the same m_z mirror eigenvalue at $k_z = \pm\pi/2$ one finds that

$$\left\langle U_{\pi/2}^{+,p} \left| m_z \left| U_{\pi/2}^{+,q} \right\rangle \right\rangle = \lambda_{m_z} \delta_{pq}, \quad \text{and thus} \quad [\mathcal{W}^+(\mathcal{L}_{k_y})]^{mn} = \left\langle U_{-\pi/2}^{+,m} \left| W^+(-\frac{\pi}{2} \leftarrow \frac{\pi}{2}) W^+(\frac{\pi}{2} \leftarrow -\frac{\pi}{2}) \right| U_{\pi/2}^{+,n} \right\rangle = \mathbb{1}^{mn}. \quad (\text{S25})$$

For a Wilson loop equal to the identity matrix all Berry phases are exactly $\theta(k_y)_i = 0$. Indeed, we see in Fig. S5(c) that the Wilson loop spectrum is generally dispersive, but is (partially) constant wherever λ_{m_z} exchange at a Dirac nodal line. Note, more complex ways in which Eq. (S24) may reduce to a diagonal matrix can also occur.

To summarize our method, it is possible to characterize a Dirac nodal line in the presence of a glide mirror symmetry by introducing a mirror-graded Wilson loop. We also find that once we consider one eigenspace of the mirror symmetry with the doubled Brillouin zone, the nodal line appears twice and each occurrence is characterized by a π Berry phase on a small loop encircling the nodal line. Nevertheless, the full information about the surface state topology is only found in the flow of the Wilson loop spectrum. Furthermore, we have shown that the mirror-graded Wilson loop spectrum is not smooth, but instead is expected to exhibit regions with constant eigenvalues in the presence of a second mirror symmetry m_z .

SV. Band topology of SmB₆

In this section we give a comprehensive topological analysis of our proposed SmB₆ model, both in the paramagnetic and magnetic phases. To do so we begin with the already known topological properties of the paramagnetic phase

and apply the methodology to our model (see Sec. [SV A](#)). We then analyze the band topology of both the A-type and G-type AFM phases (see Sec. [SV B](#) and [SV C](#)). Furthermore, we discuss the properties of the high-field phase, where all moments of SmB_6 are aligned (see Sec. [SVD](#)).

Our aim is to work out the key differences in the band topology between the paramagnetic and different magnetic phases of SmB_6 . The topological invariants, surface states and possible symmetry protected crossings are considered for the A-type and G-type phases, as well as for the high-field spin-polarized phase.

For the A-type phase we apply the previously introduced method of the mirror-graded Wilson loop (Sec. [SIV](#)). By the bulk-boundary correspondence, this relates the topology of the nodal lines in the bulk to the drumhead states at the surface. Since the formation of a magnetic order gives rise to a significant reorganization of the electronic bands, we begin each discussion with an analysis of the spatial symmetries and the back folding of the bands. This is a prerequisite for the subsequent discussion of band structures and topological invariants.

As the details of the magnetic structure are not yet experimentally determined, we have analyzed our proposed model for the possible magnetic structures with ordering vector $q = (\pi, 0, 0)$ and $q = (\pi, \pi, \pi)$, corresponding to A- and G-type orderings, respectively. We introduce the magnetic order to our model \mathcal{H} , Eq. ([S3](#)), by appropriately enlarging the unit cell and including the exchange Hamiltonian as Zeeman terms on a mean-field level. For the antiferromagnetic phases, we consider the valence state with $v = 2.74$, i.e. above a critical value of $v_c = 2.7$ for the onset of AFM order. We use the model parameters as specified in the main text and Sec. [SI](#) above.

A. Paramagnetic phase

1. Band structure of the paramagnetic phase

First, we consider the paramagnetic state with average valence $v = 2.56$, corresponding to ambient pressure. SmB_6 crystallizes in the cubic space group $Pm\bar{3}m$ (No. 221). Due to the presence of both inversion and time-reversal symmetry all bands are twofold degenerate. From the fact that this space group contains only symmorphic operations, it follows that accidental symmetry protected band crossings can only occur along fourfold and threefold rotation axes. On all other positions in k space the bands exhibit at least a small direct gap. As seen in Fig. [S1](#) there are movable Dirac points along Γ -X. The irreducible representations of the double groups at the time-reversal invariant momenta (TRIMs) Γ and R are four dimensional, which implies fourfold degeneracies (including spin) [[18](#)]. These Dirac points are slightly below the Fermi energy for the bands with f-orbital character and more than one 1 eV above the Fermi energy for the d bands. The former type of Dirac points is exceptionally massive, compared to well known examples like graphene [[19](#)] or Cd_3As_2 [[20](#)]. Note that the adjacent bands above and below the Dirac points are completely filled, thus no unusual topological transport is expected from these crossings.

2. Topological invariants of the paramagnetic phase

Due to the full band gap and time-reversal symmetry, SmB_6 can be considered as an insulator in the symmetry class AII of the Altland-Zirnbauer classification. By employing the inversion eigenvalues $\xi_n(\Gamma_i) = \pm 1$ of all the bands labeled by n at the TRIMs $\Gamma_i \in \{\Gamma, X, M, R\}$ we can assess the strong (weak) topological \mathbb{Z}_2 invariant ν_0 (ν_1, ν_2, ν_3) according to Ref. [[11](#)] by

$$(-1)^{\nu_j} = \prod_{i \in \text{TRIM}} \delta_i, \quad \text{where} \quad \delta_i = \prod_{m=1}^N \xi_{2m}(\Gamma_i), \quad (\text{S26})$$

and i labels the TRIMs of the system. The second product in Eq. ([S26](#)) is over the N occupied Kramers pairs of bands, where we note that for a given Kramers pair $\xi_{2m-1}(\Gamma_i) = \xi_{2m}(\Gamma_i)$. For the calculation of ν_0 all eight TRIMs must be used for Γ_i in Eq. ([S26](#)), whereas for the weak invariants ν_1, ν_2 , or ν_3 only the TRIMs on the planes $k_x = \pi, k_y = \pi$, or $k_z = \pi$ are considered, respectively. For both the weak and strong invariants the presence of spatial symmetries and band degeneracies simplifies the calculation. The Dirac points at Γ and R contain only bands with the same inversion eigenvalue. Thus, for an even number of filled bands (such that δ_i is well-defined at each TRIM) the respective values of δ_i are $\delta_\Gamma = \delta_R$. This applies to our model of SmB_6 , because for the above mentioned parameters two bands are occupied, and the Fermi level lies within a band gap. Due to the threefold rotation the three equivalent TRIMs corresponding to X carry the same inversion eigenvalues $\xi_n(\Gamma_i)$. The same holds for M. Thus, for the strong topological invariant ν_0 two out of the three TRIMs X and M cancel cancel in the product of δ_i . Together with the trivial contributions from the Dirac points at Γ and R the resulting strong \mathbb{Z}_2 invariant is given by $(-1)^{\nu_0} = \delta_X \delta_M$.

Band N	δ_Γ	δ_X	δ_M	δ_R	ν_3	ν_0	$\mathcal{C}_{m_z, k_z=0}$	$\mathcal{C}_{m_z, k_z=\pi}$
1	-	1	-1	-	-	-	-	-
2	1	-1	1	1	1	1	4	2
3	-	1	1	-	-	-	-	-
4	1	1	1	1	0	0	0	0

TABLE S1: Topological invariants of the paramagnetic phase. The product of all inversion eigenvalues up to the number of occupied bands (first column) are given for each TRIM in the second to the fifth column. The last four columns list the topological invariants, which characterize the occupied bands, comprising the strong \mathbb{Z}_2 invariant ν_0 , the weak \mathbb{Z}_2 invariant $\nu_1 = \nu_2 = \nu_3$, as well as the mirror Chern numbers $\mathcal{C}_{m_z, k_z=0, \pi}$.

As expected, we obtain from our tight-binding model at half filling $\nu = 1$ due to $\delta_X = -1$ and $\delta_M = 1$. In the presence of a threefold rotation around the [111] axis the weak invariants fulfill $\nu_1 = \nu_2 = \nu_3$ and are given by $(-1)^{\nu_3} = \delta_X$, because in space group $Pm\bar{3}m$ the fourfold representation at R implies $\delta_R = 1$ independently of the material. Thus, at half-filling the weak invariants $\nu_1 = \nu_2 = \nu_3 = 1$ are nontrivial, see Table S1.

Due to the presence of mirror symmetries we can also define mirror Chern numbers $\mathcal{C}_{m_z, k_z=0}$ and $\mathcal{C}_{m_z, k_z=\pi}$ within the mirror planes $k_z = 0$ and $k_z = \pi$, respectively [21]. These mirror Chern numbers are defined as $\mathcal{C}_{m_z, k_z} = \mathcal{C}_+ - \mathcal{C}_-$, where \mathcal{C}_\pm is the Chern number calculated at a fixed value of k_z within the subspace of states belonging to one mirror eigenvalue $\pm i$, see Table S1. Half of the mirror Chern number $\mathcal{C}_{m_z, k_z}/2$ is equal to the number of surface states that cross the bulk gap in the same direction. Hence, the subsystem with $k_z = 0$ exhibits two surface states, whereas for $k_z = \pi$ there is one surface state. This is consistent with the previously calculated \mathbb{Z}_2 invariants, which imply an odd (even) number of surface Dirac cones for $k_z = \pi$ ($k_z = 0$), cf. Fig. 3(g) in the main text. Note that in the presence of time-reversal symmetry the regular Chern number $\mathcal{C} = \mathcal{C}_+ + \mathcal{C}_-$ vanishes. We list all the discussed topological invariants for paramagnetic SmB₆ in Table S1.

B. A-type antiferromagnetic phase

1. Band structure of the A-type antiferromagnetic phase

In the A-type antiferromagnetic phase the regular time-reversal symmetry T is broken, but there exists a modified time-reversal operation $T_A = Tt(0, 0, 1)$, which comprises the regular time reversal T and a translation $t(0, 0, 1)$. A fixed orientation of the magnetic moments in the A-type phase removes the threefold rotation symmetry of the paramagnetic phase. The corresponding magnetic space group is $P_{2c}4/mmm'$ (No. 123.15.1013 in the OG convention). Accidental Dirac points occur only along one of the two fourfold rotation axes, i.e., on Γ -Z but not M-A, just as in the paramagnetic (and G-type) phases [22]. As discussed in Sec. SIV, the combination of inversion and time-reversal T_A leads to a twofold degeneracy of all bands.

As described in the main text and different from the G-type case there are two different band representations on the mirror plane $k_z = \frac{\pi}{2}$, where different mirror eigenvalues are paired by the combination of time reversal T_A and inversion P . This means SmB₆ in its A-type phase does not only host Dirac points on a fourfold rotation axis, but also Dirac nodal lines that are absent in the G-type phase, see Fig. S6 and Fig. 3 in the main text. Dirac points appear between bands (2, 3) and (4, 5) at the energies -62 meV and -37 meV, respectively, below the Fermi level.

Additionally, there are accidental but symmetry-protected nodal lines around the A point between the bands (2, 3) and close to the Z and R points between the bands (4, 5). The latter nodal lines are close to the Fermi energy and are partially of type II. These type-II nodal lines exhibit tilted bands along some radial cuts of the band structure intersecting the nodal line, while in the direction orthogonal to both the mirror plane and the nodal line, i.e., along k_z they exhibit regular cone-like dispersions [23]. The nodal lines near R are weakly dispersive spreading from -6 meV to 5 meV in energy. Near Z the nodal lines are effectively dispersionless, covering energies from -32 meV to -31 meV. Both types of nodal lines have a diameter of up to one fifth of the Brillouin zone (see Fig. 3(c) of the main text).

2. Topological invariants of the A-type antiferromagnetic phase

We group our discussion of the topological invariants according to the associated surface states that appear on the [010] and [001] surfaces, as discussed in the main text.

Topology of [010] surface states.— To assess the topology relevant for the [010] termination we consider two invariants that can be defined for the $k_z = 0$ plane. We note that for SmB₆ in the A-type AFM phase there exists a full

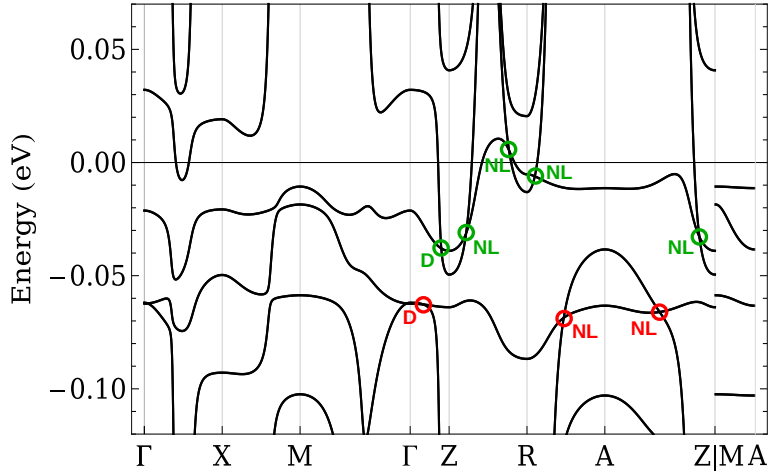


FIG. S6: Bandstructure of SmB_6 in the A-type antiferromagnetic phase. The circles indicate Dirac points (D) and nodal lines (NL), where the colors red and green indicate crossings between bands (2,3) and (4,5), respectively, as in Fig. 3 of the main text.

Band N	Γ	X	M	ν_3	\mathcal{C}_m
1	1	1	-1	1	6
2	-1	-1	1	1	6
3	1	1	-1	1	2
4	-1	-1	1	1	6
5	1	1	1	0	4

TABLE S2: Topological invariants of the A-type antiferromagnetic phase. Inversion eigenvalues at the TRIMs are given in columns 2, 3, and 4, for the different band fillings. ν_3 denotes the weak \mathbb{Z}_2 invariant associated to the plane $k_z = 0$. In the last column the mirror Chern numbers \mathcal{C}_m are given for the $k_z = 0$ plane for fillings up to the band given in the first column.

gap between the fourth and the fifth band in the $k_z = 0$ plane, see Fig. S6. Hence, for this filling we can define in the $k_z = 0$ plane a weak \mathbb{Z}_2 invariant ν_3 as well as a mirror Chern number \mathcal{C}_{m_z} . First we note that the gapped plane $k_z = 0$ can be understood as an antiferromagnetic topological insulator characterized by the weak \mathbb{Z}_2 invariant ν_3 [24]. This is possible because within the $k_z = 0$ plane the time-reversal operation $T_A = Tt(0, 0, 1)$ behaves identically to the regular time reversal T . As for the paramagnetic phase, Sec. SV A 2, we determine ν_3 from the inversion eigenvalues [11]. Assuming that the lowest four bands are filled, we find $\nu_3 = 1$ indicating a topological gap in the $k_z = 0$ plane. This comes as no surprise, since the paramagnetic phase of SmB_6 is also nontrivial with $\nu_3 = 1$, cf. Table S1. During the magnetic transition between these two phases the inversion eigenvalues of the plane with $k_z = \pi$ are folded back to the $k_z = 0$ plane, and thus every second band gap within the $k_z = 0$ plane is topologically nontrivial in the A-type AFM phase [24]. In addition, it turns out that also for the odd band gaps (i.e., for an odd number of filled bands), the weak invariant ν_3 is nontrivial, with the exception of the gap between band 5 and 6, see in Table S2. Note, that the contribution of the TRIM X to ν_3 cancels since it occurs in two copies related by the fourfold symmetry. Furthermore, we remark that the Kramers pairs at the TRIMs within the $k_z = \pi$ plane (i.e., at Z, R and A) consist of two states with different inversion eigenvalues, as a result of the time-reversal operation T_A . As a consequence, the invariants ν_i corresponding to the planes $k_x = 0, \pi$, $k_y = 0, \pi$, and $k_z = \pi$ are ill-defined, which agrees with the deviation from the AII topological classification due to $T_A^2 = +1$ at $k_z = \pi$.

Second, we note that within the mirror plane $k_z = 0$ the mirror Chern number \mathcal{C}_{m_z} can be defined, since within this plane PT_A pairs different m_z mirror eigenvalues. The values of the mirror Chern number $\mathcal{C}_{m_z} = \mathcal{C}_+ - \mathcal{C}_-$ are given in Table S2. We note that for all considered band fillings the mirror Chern number is nonzero, while the total Chern number $\mathcal{C} = \mathcal{C}_+ + \mathcal{C}_-$ is always zero. Bands with a non-zero value of the mirror Chern number are expected to exhibit surface states for lattice terminations that do not break the mirror symmetry m_z , e.g., the [010] termination. The two topological invariants, ν_3 and \mathcal{C}_{m_z} , both describe the $k_z = 0$ plane and are consistent. If $\mathcal{C}_{m_z}/2$ is odd and there must be an odd number of surface states that cross the bulk band gap, then the weak \mathbb{Z}_2 invariant is always nontrivial, i.e. $\nu_3 = 1$. For band 5 the mirror Chern number predicts an even number of surface states, which is in agreement with $\nu_3 = 0$.

The surface states for the [010] termination as function of energy and surface momentum k_x are shown in Fig. 3(g)

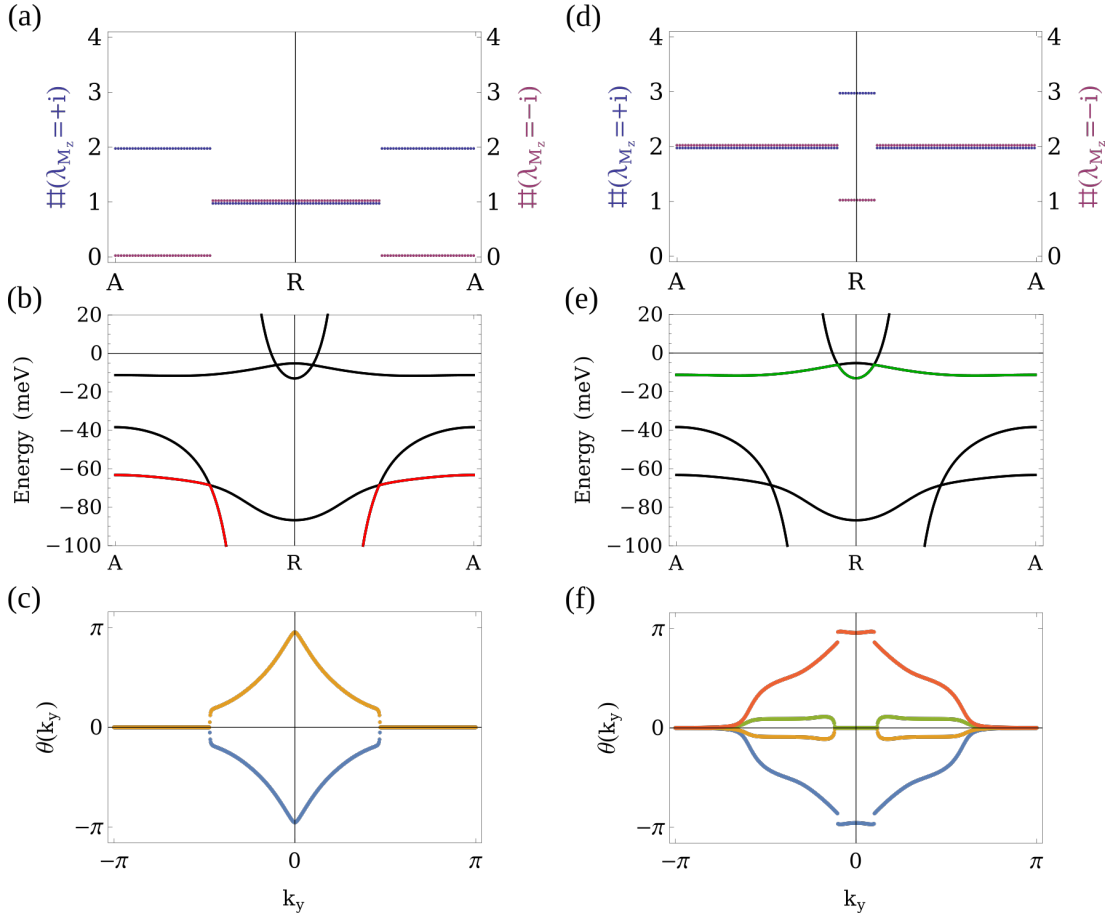


FIG. S7: Relation of mirror eigenvalues, nodal lines, and the spectral flow of the Wilson matrix in the A-type antiferromagnetic phase. (a-c) two occupied bands, (d-f) four occupied bands. (a,d) Multiplicity of mirror eigenvalues for the occupied bands not including the twofold degeneracy due to the PT_A symmetry. (b,e) Band structure, the considered band is highlighted with red (green) corresponding to band 2 (4). (c,f) Phases of the mirror-graded Wilson loop spectra as a function of k_y , for loops along the k_z direction with fixed $k_x = \pi$.

of the main text. We observe a non-trivial surface state connecting bulk and valence bands with a different number of surface Dirac cones at $\bar{\Gamma}$ than at \bar{X} , in full agreement with the weak \mathbb{Z}_2 invariant $\nu_3 = 1$ (see Table S2 and the black arrows in Fig. 3(g) of the main text). Within the gap between bands 4 and 5, we observe three surface states, in agreement with the mirror Chern number $\mathcal{C}_{m_z} = 6$. We note that a nontrivial \mathbb{Z}_2 invariant has also been found for a related model in Ref. [21], whereas we obtain larger values of the mirror Chern number enabled by the increased number of bands stemming from the relevant e_g and Γ_8 quartet. The mirror Chern numbers of the paramagnetic phase at half filling add up to the mirror Chern number of the A-type phase of the $k_z = 0$ plane, which corresponds to how the \mathbb{Z}_2 invariants of the paramagnetic and antiferromagnetic phase have been found to be related above. This concludes our analysis of the topological invariants relevant to the [010] surface termination.

Topology of [001] surface states.— Next, we consider the bulk topology relevant for the [001] termination. First, we consider the distinguishing feature of the A-type magnetic order, i.e., the emergence of mirror symmetry protected nodal lines. The nodal lines on the plane $k_z = \pi/2$ have a codimension $p = d - d_{FS} = 2$. Further, time reversal T_A anticommutes with the mirror symmetry m_z , while squaring to $T_A^2 = +1$. This classifies these nodal lines in the presence of such a mirror symmetry m_z as class AI, and they are thus trivial for $p = 2$ [25]. However, we note that in the cited classification scheme the present nodal line shape has not been considered [25]. Thus, a closer consideration is needed. The mirror symmetry m_z protects the nodal lines and its eigenvalues λ_{m_z} can be used to label the bands. The values of the mirror eigenvalues λ_{m_z} are shown in Fig. S7(a,d). At the nodal lines mirror eigenvalues cross, which is reflected in the mirror-graded Wilson loop spectrum, see below.

We find that the surface states visible in Fig. 3(e) in the main text can be inferred from the Wilson loop spectrum with periodic boundary conditions. The Wilson loop spectrum is calculated on mirror planes left invariant by \hat{m}_x

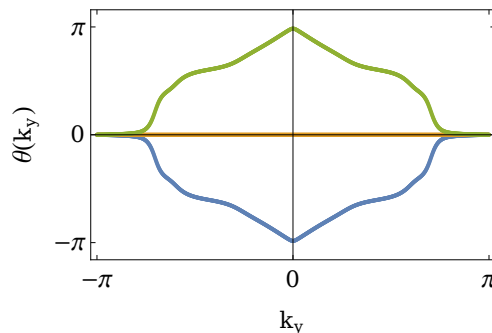


FIG. S8: Mirror-graded Wilson loop spectrum for three occupied bands in the proximity of an avoided crossing. Wilson loop along the k_z direction at $k_x = \pi$ as function of k_y . The rapid change in the spectrum coincides with a weakly gapped bulk band crossing, cf. surfaces states in Fig. 3(e) (blue arrow) of the main text.

and \tilde{m}_y , which are glide mirror symmetries with a translation along the [001] direction. In the matrix block of one mirror eigenvalue $H^+(\mathbf{k})$ all nodal lines are singly degenerate and thus it is possible to determine a Berry phase on a small loop enclosing each nodal line. The result is a π Berry phase for each of the nodal lines. Yet, this is insufficient to make the actual connection to the surface states, because a quantization of the Berry phase leaves a dependence on the chosen surface termination.

To reach a comprehensive description we thus employ the methodology introduced in Sec. SIV and determine the Wilson loop spectrum for loops along the k_z direction at fixed k_x and variable k_y . In Fig. S7 the analysis is exemplarily shown for the $k_x = \pi$ plane, which determines the surface state along the line $\bar{X}-\bar{M}$, see Fig. 3(e) in the main text.

For two occupied bands, see Fig. S7(a-c) there is an extended region, where all bands are described by a single mirror eigenvalue, $\lambda_{m_z} = +i$. As a result the Wilson loop spectrum is pinned to $\theta = 0$ as shown before in Sec. SIV. Starting at the nodal line there is a rapid change in the Wilson loop spectrum, which is accompanied by a surface state in the gap between the second and third band as discussed in the main text and Fig. 3(e) (red arrow).

For four occupied bands, see Fig. S7(d-f), bands of both mirror eigenvalues are always occupied. Nevertheless, on one side of the nodal line a constant Wilson loop eigenvalue with the phase $\theta = \pi$ emerges and the flow of eigenvalues corresponds to the presence of surface states, as seen in Fig. 3(e) (green arrow) of the main text. To support the bulk origin of these surface states, we have confirmed that a featureless potential term applied to the surface of the open system does not remove the surface states.

Finally, a comment is in place regarding the prominent surface state between the third and fourth band on the line $\bar{X}-\bar{M}$, see Fig. 3(e) (blue arrow) of the main text, which appears to end at an avoided crossing of the bulk spectrum, see Fig. S6. Note, the crossing is avoided because on the $k_z = 0$ plane no symmetry protects band crossings. Although the crossing is gapped, it exhibits smooth features in the Wilson loop spectrum, which are similar to those at nodal lines, see Fig. S8, i.e., there are nearly flat bands within a region demarcated by the nodal line. The existence of this feature can be understood from the backfolding of bands for the magnetic unit cell, but unlike for the nodal lines the mirror symmetry m_z is insufficient to protect the crossing. There is also no \mathbb{Z}_2 invariant that could be associated to these gapped Dirac surface states, because on the plane $k_x = \pi$ the relation $T_A^2 = -1$ does generally not hold.

C. G-type antiferromagnetic phase

1. Band structure of the G-type antiferromagnetic phase

The onset of the magnetic order increases the unit cell size and reduces the time-reversal symmetry to the operation $T_G = Tt(1, 0, 0)$ with $T = i\sigma_y K$ and the complex conjugation K . This corresponds to the space group $P14/mmm'$ (No. 123.19.1017 in the OG convention). Since the threefold rotation symmetry is broken by the magnetic order, crossings of higher degeneracies may only occur along the remaining fourfold rotation axis Γ -Z, see Fig. S9. Dirac points at TRIMs present in the paramagnetic phase are gapped in the magnetic phase [22]. Notably, unlike for the A-type case, there is no band crossing near the Fermi level for the G-type antiferromagnetic phase.

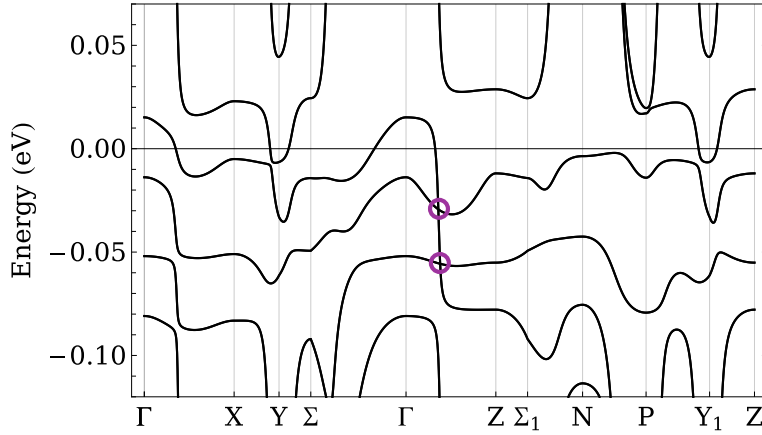


FIG. S9: Bandstructure of SmB₆ in the G-type antiferromagnetic phase. The purple circles highlight the Dirac points that are shown in Fig. 3(d) of the main text.

Band N	Γ	X	Z	$\nu_1 = \nu_2 = \nu_3$	\mathcal{C}_m
1	-1	1	1	1	6
2	1	-1	-1	1	10
3	-1	1	1	1	2
4	1	-1	-1	1	6
5	1	1	1	0	4

TABLE S3: Topological invariants of the G-type antiferromagnetic phase. Inversion eigenvalues at the TRIMs are given from the second to the fourth column taking into account all bands up to the one labeled in the first column. ν_1, ν_2, ν_3 denote the weak \mathbb{Z}_2 invariant associated to the plane $k_x = 0, k_y = 0$ and $k_z = 0$, respectively. In the last column the mirror Chern numbers \mathcal{C}_m are given for the $k_z = 0$ plane.

2. Topological invariants of G-type antiferromagnetic phase

The Brillouin zone geometry of the G-type magnetic order allows for the definition of three weak \mathbb{Z}_2 invariants ν_1, ν_2 , and ν_3 , even though time-reversal symmetry is broken. This is different to the A-type antiferromagnetic phase, where only ν_3 can be defined. Interestingly, while each of the weak invariants is determined on a different plane defined by $k_x = 0, k_y = 0$, or $k_z = 0$, for all three indices the inversion eigenvalue formula uses the same TRIMs. The latter statement is evident from the body-centered Brillouin zone shown in Fig. 3(d) of the main text, where all mirror planes contain the same points, i.e., Γ, X and Z . Nevertheless, the nonsymmorphic nature of the time-reversal symmetry prevents the definition of the strong invariant ν , because only at Γ, X and Z the necessary condition $T_G^2 = -1$ holds, while at the TRIM N one finds $T_G^2 = +1$. The inversion eigenvalues for the former TRIMs are listed in Table S3. The weak invariants ν_i can be determined using $(-1)^{\nu_i} = \delta_\Gamma \delta_Z$, where the point X drops out due to its even multiplicity. Thus, one finds that for fillings 1, 2, 3, and 4, the weak invariants are nontrivial, while for filling 5 they are trivial. In the surface band structure for the G-type case the bands overlap, see Fig. 3(f,h) in the main text. Nevertheless, for the $[001]$ termination in the vicinity of the Fermi energy the overlap of bands is sufficiently small so that one can confirm the correspondence between the invariant and the surface spectrum.

As before we refine this analysis using crystalline topological invariants. We will use the symmorphic mirror symmetry m_z and that the Hamiltonian is gapped on the $k_z = 0$ mirror plane. The mirror Chern number \mathcal{C}_m is consistent with the weak invariant ν_3 , see Table S3, and it is at the Fermi energy identical to the A-type phase. If only two (or three) bands are occupied and the fourfold rotation symmetry is unbroken, then there are two Dirac points on the axis Γ - Z , hence a mirror Chern number is not well-defined on the planes $k_x = 0$ and $k_y = 0$. While the same is technically true for the \mathbb{Z}_2 invariant, we can already determine their values from inversion eigenvalues assuming weakly gapped Dirac nodes. The latter is not possible for the A-type antiferromagnetic phase, where the relevant mirror planes, $k_x = 0$ and $k_y = 0$, fall into a trivial topological class even if the bands would be gapless.

To further analyze the surface states at $k_{x,y} = 0$, let us consider the spectral flow of Wilson loop eigenvalues in the subspace of one eigenvalue of mirror symmetry. Due to the Brillouin zone's extension along k_z the technically nonsymmorphic glide mirror symmetries \tilde{m}_x and \tilde{m}_y do not lead to an exchange of the mirror eigenvalues when moving from $k_z = -\pi$ to $k_z = +\pi$. Hence, we do not need to use our mirror-graded Wilson loop formalism, but can just

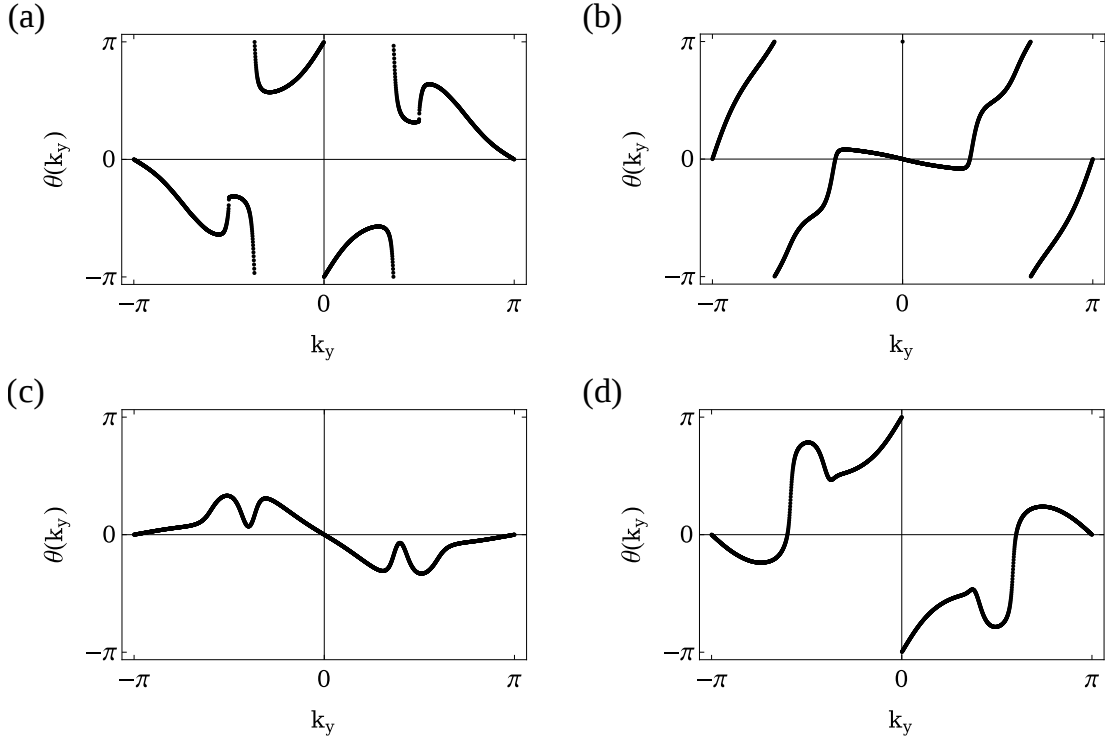


FIG. S10: Mirror Berry phase winding of SmB_6 in the G-type antiferromagnetic phase. (a)-(d) correspond to the case of 1 to 4 occupied bands, respectively. The non-Abelian mirror Berry phase $\theta(k_y)$ is computed as a function of k_y , for closed loops in the k_z -direction at constant $k_x = 0$. The mirror Berry phases wind once (a,d) or twice (b). At $k_y = 0$ (b) and (c) are only well-defined in the absence of the Dirac points on the Γ -Z axis.

consider a regular mirror Berry phase, which is the sum of all phases of Wilson loop eigenvalues. The non-Abelian mirror Berry phases for loops along the k_z axis within the $k_x = 0$ plane as function of k_y are given in Fig. S10. We find a winding corresponding to a mirror Chern number of $\mathcal{C}_m^x = -1, +2, 0, +1$ for the case of one up to four occupied bands. While the mirror Berry phase is continuous in Fig. S10, this is not necessarily true if we assume a different orientation of loops within the same mirror plane. By taking loops along k_y with a mirror Berry phase as function of k_z , one finds jumps in the Berry phase at the positions of the Dirac points. If the fourfold symmetry is broken by some perturbation, then these jumps become smooth and the mirror Chern numbers take the values we have given above independently of the orientation of Wilson loops.

To summarize the analysis of the G-type order, we find that unlike for the A-type phase all weak invariants are well-defined and instead of nodal line surface states the [001] termination exhibits a surface Dirac cone, see the black arrow at $E = 18$ meV in Fig. 3(f).

D. High-field limit

1. Band structure in the high-field limit

For sufficiently strong external magnetic fields the magnetic moments become fully polarized. Here, we study the case when the field is along the z direction such all moments point along z. The magnetic space group for this case is $P_4/m\bar{m}'m'$ (No. 123.7.1005 in the OG convention). This is a symmorphic space group, where only inversion, the mirror symmetry m_z , and rotations with respect to the z-axis remain as unitary symmetries. We can thus expect to find accidental nodal lines in the mirror planes $k_z = 0, \pi$ and Weyl points characterized by an exchange of rotation eigenvalues along the paths Γ -Z, X-R and M-A. In Fig. S11 the band structure is shown for our model, which exhibits nodal lines in the $k_z = 0$ and $k_z = \pi$ planes, and several Weyl points on all four remaining rotation axes. An overview of all Weyl points and twofold nodal lines is given in Fig. S12.

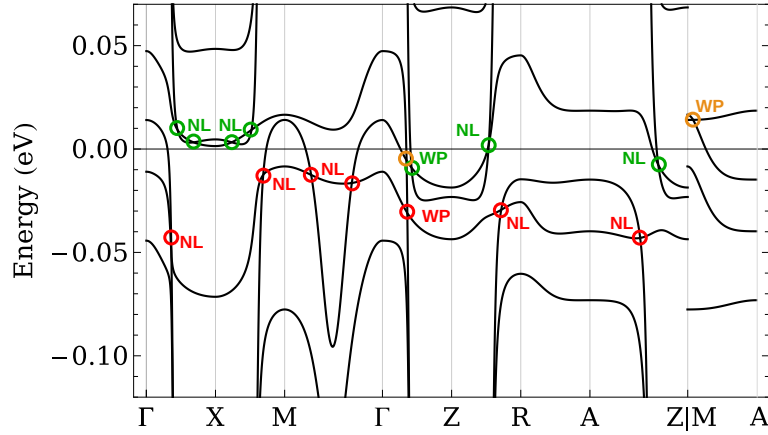


FIG. S11: Bandstructure of SmB_6 with valence 2.73 assuming moments aligned along z direction. The red, orange and green circles highlight the Weyl points and nodal lines. The red, orange and green color corresponds to band crossings between bands (2,3), (3,4), and (4,5), respectively.

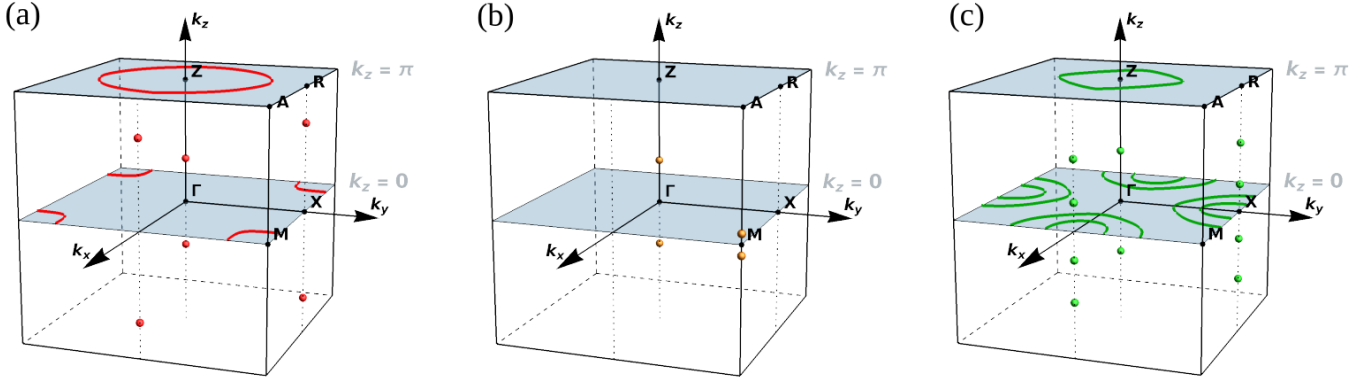


FIG. S12: Point and line crossings in spin-polarized SmB_6 with valence 2.73. (a) red, (b) orange and (c) green coloring highlights the Weyl points and nodal lines between bands (2,3), (3,4), and (4,5), respectively, see also Fig. S11.

2. Topological invariants in the high-field limit

For the spin-polarized case the band structure has several Weyl points of varying separation as well as nodal lines. To characterize the Weyl points we consider their chiralities and their effect on the total Chern number calculated on planes of constant k_z . In Fig. S13 we present the Chern numbers evaluated on planes perpendicular to k_z for two, three and four filled bands. Jumps of the Chern number occur only at the positions of the identified Weyl points with two exceptions. In Fig. S13(b) two additional jumps can be found. Generally additional accidental Weyl points occur in a group comprising four Weyl points of identical unit charge at a given value of k_z due to the crystalline symmetries. Interestingly, the accidental Weyl points nearly coincide with a jump due to the double Weyl point along the M-A line from -2 to -4, which is followed by the change in the Chern number from -4 to 0. Such jumps in the Chern number can only be explained by the presence of the discussed four accidental Weyl points at generic positions situated at $k_z \approx \pm 0.3$ between the bands 3 and 4. The second case of four Weyl points at generic positions is seen in Fig. S13(c), where the jump at $k_z \approx \pm 0.5$ does not correspond to any crossing on one of the rotation axes.

The Weyl points occur on both the twofold and the fourfold rotation axes and their charges are either one or two. The latter ones (i.e. double Weyl points) are protected by the four fold rotation symmetry. There are six Weyl points between the bands 2 and 3 with charge 1. For the bands 3 and 4 only four double Weyl points occur, two on each of the fourfold rotation axes as well as four pairs of single Weyl points at generic positions. Notably, the region of non-zero Chern number spans nearly the full Brillouin zone and, unlike for bands 2 and 3, the Chern number occurs effectively with a single sign, such that the contribution from different k_z to the topological responses would add

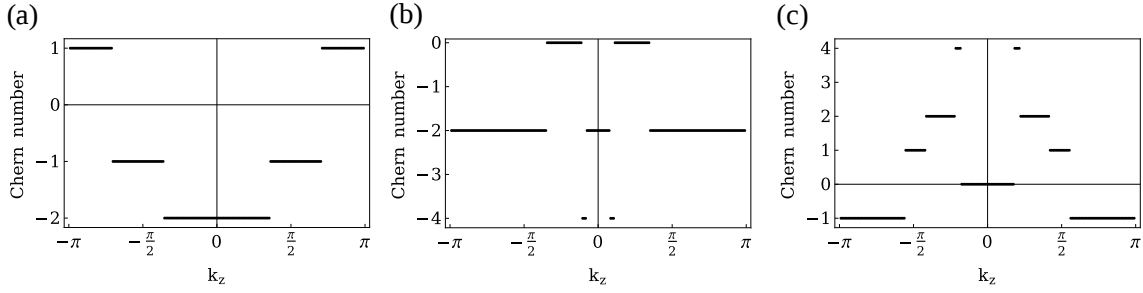


FIG. S13: Chern numbers for spin-polarized SmB₆ calculated on planes of constant k_z . (a),(b),(c) display the Chern numbers for fillings up to the second, third, and fourth band, respectively.

up. To reach a quantitative statement regarding the topological responses, for example the anomalous Hall effect, a detailed calculation of the topological contributions by taking the partial filling of bands into account is required, but this is beyond the scope of this manuscript. The Chern number between bands 4 and 5 takes five different values, a result of the 18 Weyl points including 8 at generic positions.

Besides the Weyl points, there are also twofold degenerate nodal lines that are protected by the symmorphic mirror symmetry m_z . Since the bands are nondegenerate almost everywhere, all nodal lines exhibit a quantized Berry phase of $\theta = \pi$ on any path encircling a single line. Notably, nodal lines occur together with some of the Weyl points in the vicinity of the Fermi level.

-
- [1] N. P. Butch, J. Paglione, P. Chow, Y. M. Xiao, C. A. Marianetti, C. H. Booth, and J. R. Jeffries, *Phys. Rev. Lett.* **116**, 156401 (2016).
- [2] G. Sawatzky and R. Green, in *Quantum Materials: Experiments and Theory*, edited by E. Pavarini, E. Koch, J. van den Brink, and G. Sawatzky (Forschungszentrum Jülich, 2016, ISBN 978-3-95806-159-0).
- [3] A. Amorese, O. Stockert, K. Kummer, N. B. Brookes, D.-J. Kim, Z. Fisk, M. W. Haverkort, P. Thalmeier, L. H. Tjeng, A. Severing, *Phys. Rev. B* **100**, 241107(R) (2019).
- [4] J. C. Slater and G. F. Koster, *Phys. Rev.* **94** 1498 (1954).
- [5] K. Takegahara, Y. Aoki, and A. Yanase, *J. Phys. C* **13** 583 (1980).
- [6] T. Takimoto, *J. Phys. Soc. Jpn.* **80**, 123710 (2011).
- [7] P. P. Baruselli and M. Vojta, *Phys. Rev. B* **90**, 201106(R) (2014).
- [8] M. Neupane, N. Alidoust, S.-Y. Xu, T. Kondo, Y. Ishida, D. J. Kim, C. Liu, I. Belopolski, Y. J. Jo, T.-R. Chang, H.-T. Jeng, T. Durakiewicz, L. Balicas, H. Lin, A. Bansil, S. Shin, Z. Fisk, and M. Hasan, *Nat. Commun.* **4**, 2991 (2013).
- [9] Y. Nakajima, P. Syers, X. Wang, R. Wang, and J. Paglione, *Nat. Phys.* **12**, 213 (2016).
- [10] A. Aishwarya, Z. Cai, A. Raghavan, M. Romanelli, X. Wang, X. Li, G. D. Gu, M. Hirsbrunner, T. Hughes, F. Liu, L. Jiao, and V. Madhavan, *Science* **377**, 1218 (2022).
- [11] L. Fu and C. L. Kane, *Phys. Rev. B* **76**, 045302 (2007).
- [12] J. C. Y. Teo, L. Fu, and C. L. Kane, *Phys. Rev. B* **78**, 045426 (2008).
- [13] F. Zhang, C. L. Kane, and E. J. Mele, *Phys. Rev. Lett.* **111**, 056403 (2013).
- [14] Y. Hatsugai, *J. Phys. Soc. Jpn.* **74**, 1374 (2005).
- [15] A. Alexandradinata, X. Dai, and B. A. Bernevig, *Phys. Rev. B* **89**, 155114 (2014).
- [16] L. Fidkowski, T. S. Jackson, and I. Klich, *Phys. Rev. Lett.* **107**, 036601 (2011).
- [17] D. Vanderbilt, *Berry phases in electronic structure theory* (Cambridge University Press, 2018).
- [18] L. Elcoro, B. Bradlyn, Z. Wang, M. G. Vergniory, J. Cano, C. Felser, B. A. Bernevig, D. Orobengoa, G. d. l. Flora, and M. I. Aroyo, *J. Appl. Cryst.* **50**, 1457 (2017).
- [19] K. S. Novoselov, A. K. Geim, S. V. Morozov, D. Jiang, M. I. Katsnelson, I. V. Grigorieva, S. V. Dubonos, and A. A. Firsov, *Nature* **438**, 197 (2005).
- [20] M. Neupane, S.-Y. Xu, R. Sankar, N. Alidoust, G. Bian, C. Liu, I. Belopolski, T.-R. Chang, H.-T. Jeng, H. Lin, A. Bansil, F. Chou, and M. Z. Hasan, *Nat. Commun.* **5**, 1 (2014).
- [21] K. Kimura, T. Yoshida, and N. Kawakami, *J. Phys. Soc. Jpn.* **87**, 084705 (2018).
- [22] L. Elcoro, B. J. Wieder, Z. Song, Y. Xu, B. Bradlyn, and B. A. Bernevig, arXiv:2010.00598 (2020).
- [23] J. He, X. Kong, W. Wang, and S.-P. Kou, *New J. Phys.* **20** 053019 (2018).
- [24] R. S. K. Mong, A. M. Essin, and J. E. Moore, *Phys. Rev. B* **81**, 245209 (2010).
- [25] C.-K. Chiu and A. P. Schnyder, *Phys. Rev. B* **90**, 205136 (2014).